Constraining ALP-nucleon interactions via the diffuse flux of MeV ALPs from galactic supernovae

Marina Cermeño Gavilán

Institute of Theoretical Physics (IFT UAM/CSIC)

D. Alonso-González, D. Cerdeño, **M. Cermeño**, A. D. Perez, PRD 111 (2025) 083019

May 27, 2025

CSIC
Consejo Superior de Investigaciones Científicas

EXCELENCIA SEVERO OCHOA

COSMIC WISPERS
CA21106

Detection of axion-like particles from supernovae

- **Axion**: pseudoscalar Nambu-Goldston boson from the Peccei-Quinn mechanism, solves the strong CP problem *Peccei and Quinn, PRL 38 (1977) 1440*
- **Axion-like particle (ALP)**: pseudoscalar Nambu-Goldston boson from Standard Model extensions

Axions and ALPs interacting with nucleons ⇒ supernova (SN) production

MeV ALPs constitute a galactic diffuse SN background that can be probed in neutrino water Cherenkov detectors via $a\,p \to p\,\gamma$ with $E_\gamma \sim 30$ MeV

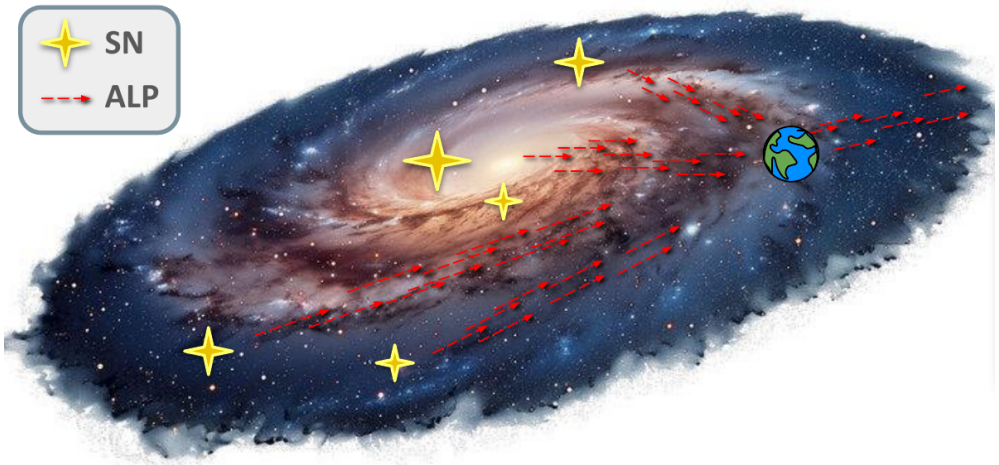

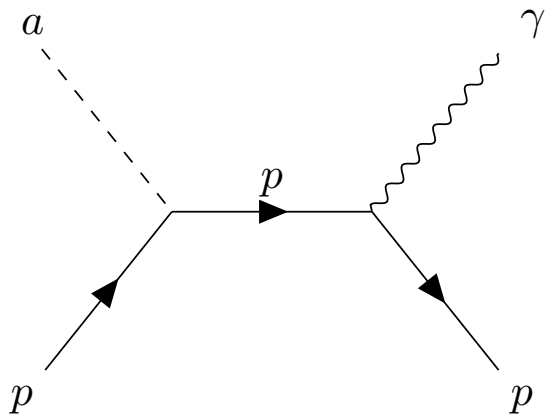

Core-collapse supernovae

SN are violent stellar phenomena happening when stars with $M > 8\,M_\odot$ have burned out their nuclear fuel ⇒ gravitational core collapse ⇒ proto-neutron star (proto-NS)

In the first seconds after explosion, the proto-NS core ($R \sim 20$ km) reaches $T \sim 30$ MeV and $\rho \sim 10^{14} - 10^{15}$ g/cm^3

Fischer et al., PRD 85 (2012) 083003

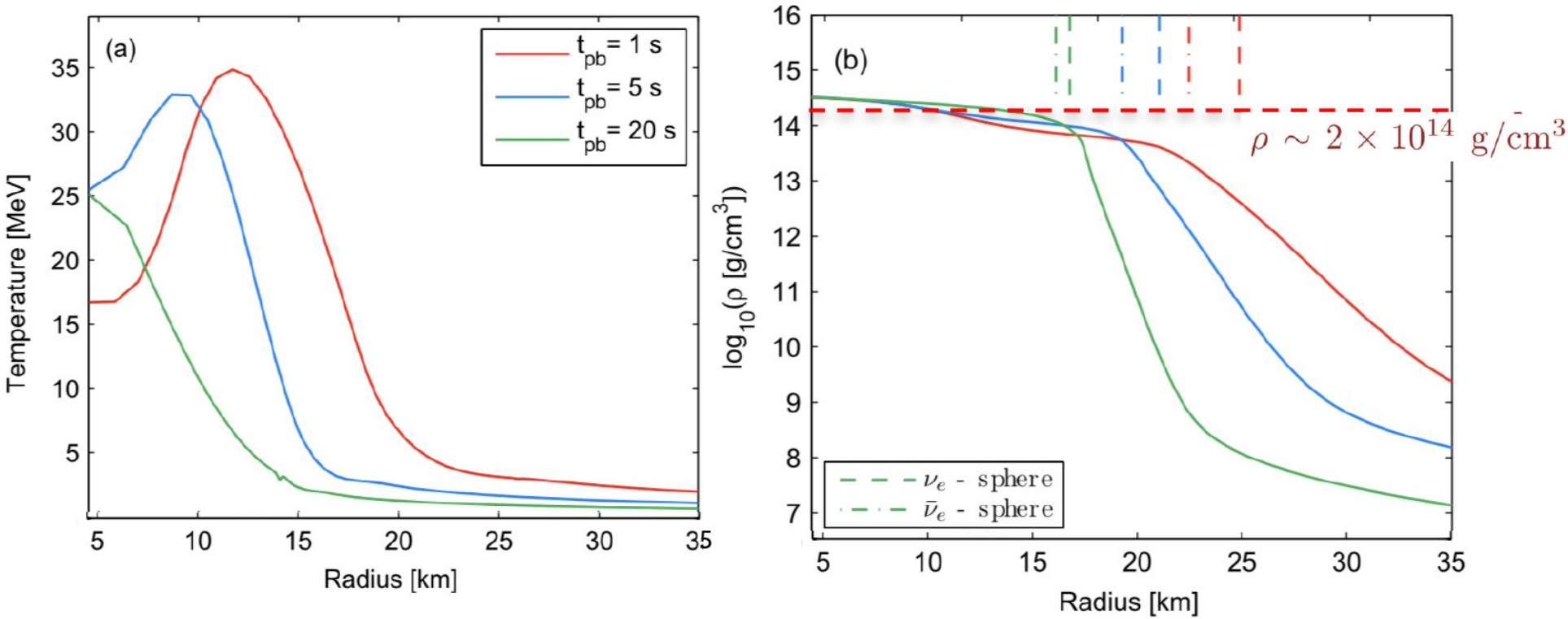

Proto-NS composition

$n_B = n_n + n_p = \frac{\rho}{m_N}$, the nuclear saturation density $n_0 = 0.15\ \mathrm{fm}^{-3}$

$$n_p = n_{e^-} + n_{\mu^-} + n_{\pi^-}, \quad n_{\pi^+} \ll n_{\pi^0} \ll n_{\pi^-}, \ \frac{n_{\pi^0}}{n_{\pi^-}} \sim \frac{n_{\pi^+}}{n_{\pi^0}} \sim \frac{n_p}{n_n} = O(0.1)$$

Fore, Reddy, PRC 101 (2020) 035809 (solid lines with pions)

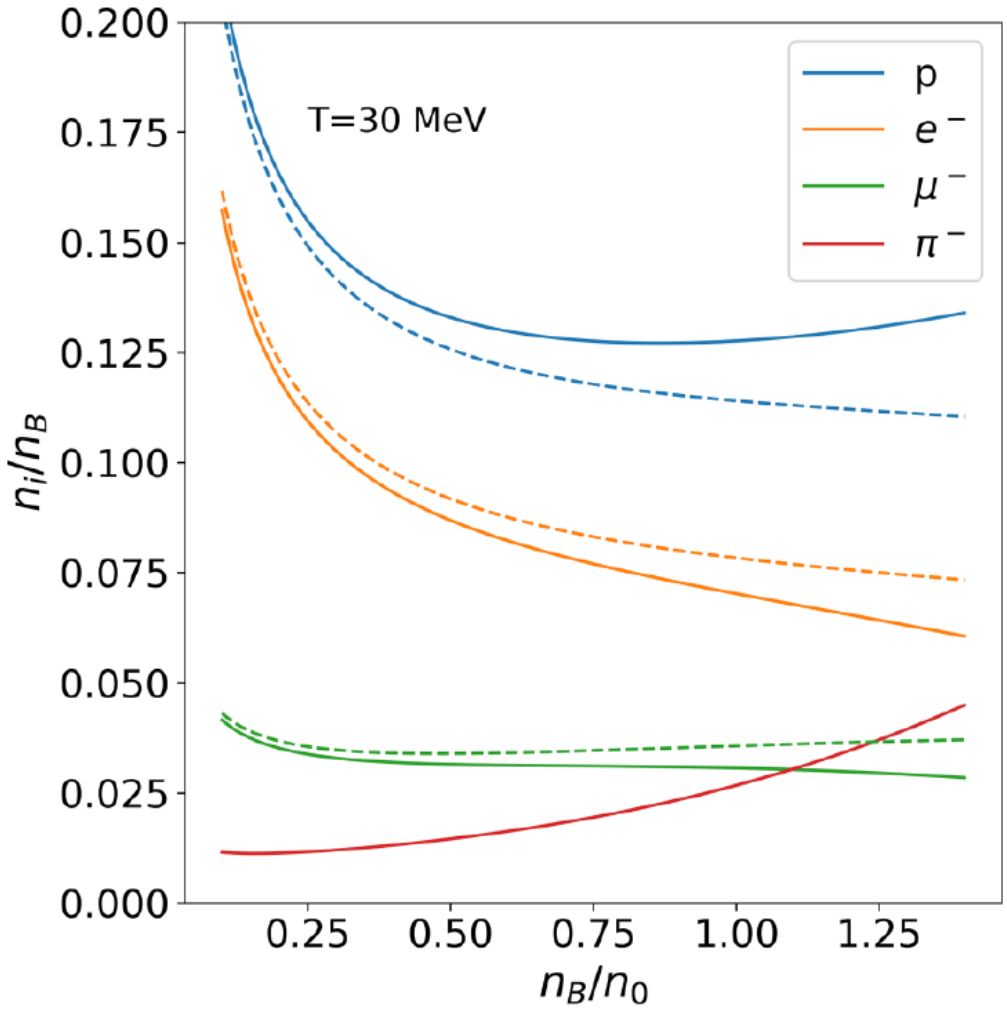

ALP-nucleon interactions

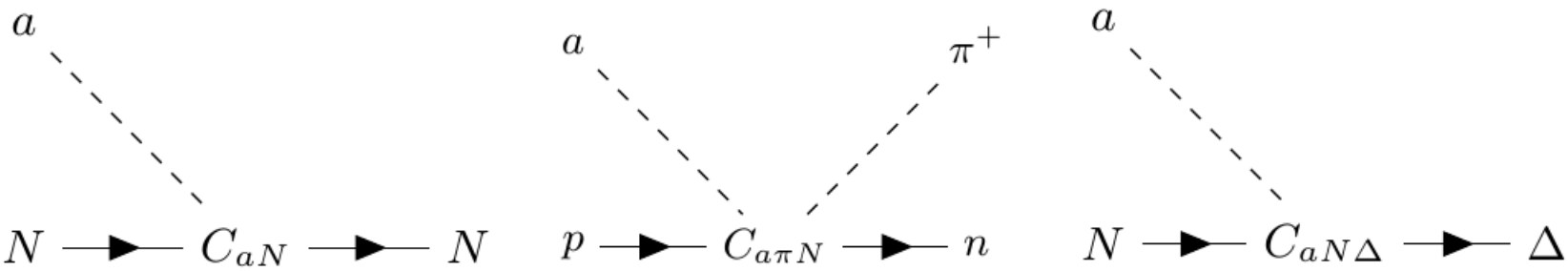

Di Luzio et al., Phys. Rep. 870 (2020) 1, Chang, Choi, PLB 316 (1993) 51

$$\begin{aligned}\mathcal{L}_{int} &= g_a \frac{\partial_\mu a}{2\, m_N} \Big[C_{ap}\, \bar{p}\, \gamma^\mu\, \gamma_5\, p + C_{an}\, \bar{n}\, \gamma^\mu\, \gamma_5\, n + \\ &\frac{C_{a\pi N}}{f_\pi}\, \left(i\, \pi^+\, \bar{p}\, \gamma^\mu\, n - i\, \pi^-\, \bar{n}\, \gamma^\mu\, p \right) + \\ &C_{aN\Delta}\, \left(\bar{p}\, \Delta^+_\mu + \bar{\Delta}^+_\mu\, p + \bar{n}\, \Delta^0_\mu + \bar{\Delta}^0_\mu\, n \right) \Big]\end{aligned}$$

C_{aN} model-dependent $O(1)$ axion-nucleon coupling, $g_{aN} = g_a C_{aN}$, $N = p, n$

$C_{a\pi N} = (C_{ap} - C_{an})/\sqrt{2} g_A$, $C_{aN\Delta} = -\sqrt{3}/2 (C_{ap} - C_{an})$

$g_A \simeq 1.28$ the axial coupling, $f_\pi = 92.4$ MeV pion decay constant

ALP-nucleon bounds

Benchmark values $C_{ap} = -0.47$, $C_{an} = 0$, inspired by the Kim-Shifman-Vainshtein-Zakharov (KSVZ) axion model *Grilli di Cortona, et al., JHEP 01 (2016) 034*; $g_{ap} = C_{ap} g_a$

Lella et al., PRD 109 (2024) 023001

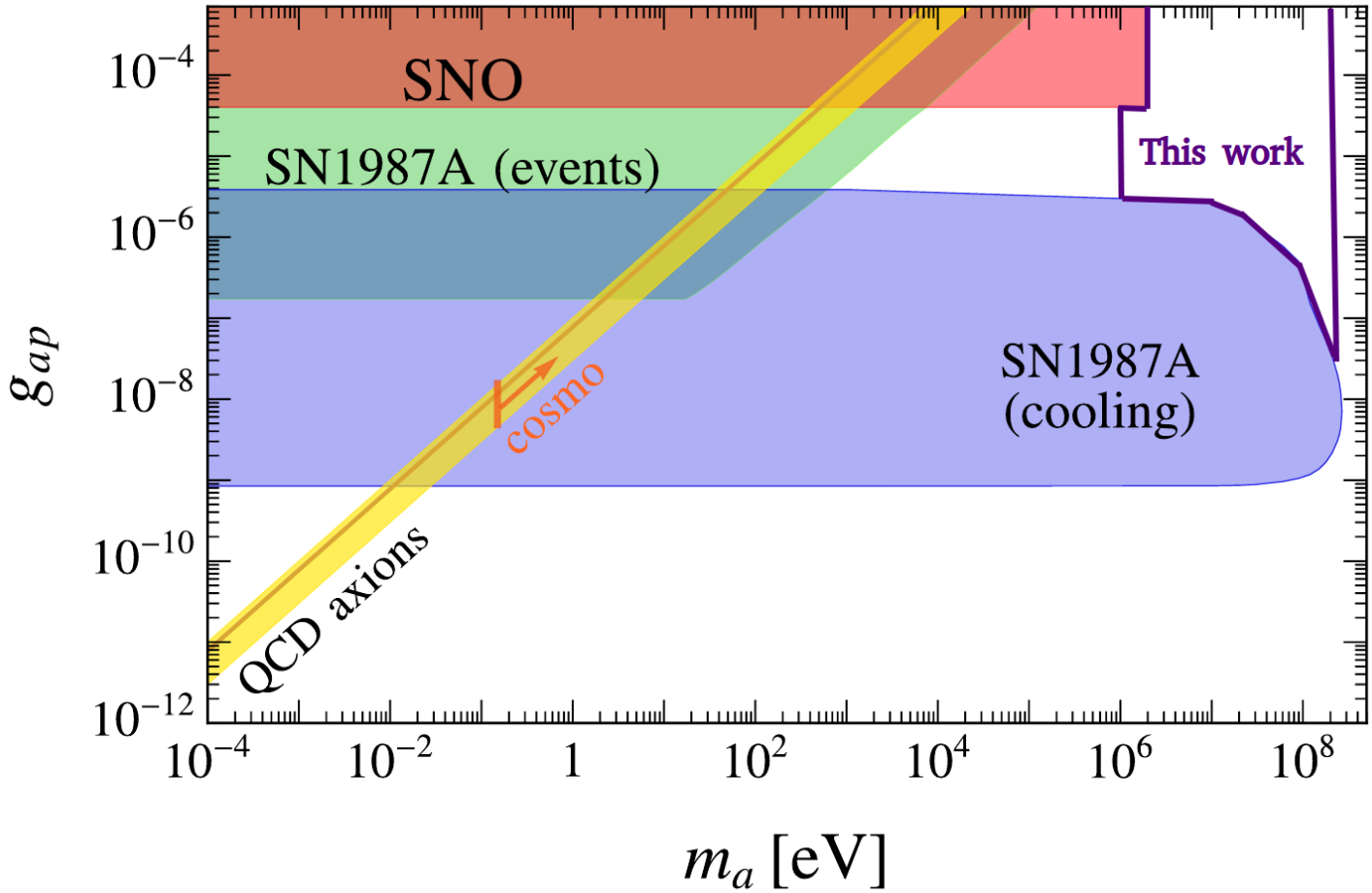

- $m_a \lesssim 1$ MeV, no galactic diffuse background
- $m_a \gtrsim 200$ MeV, no SN production

ALP production in SN

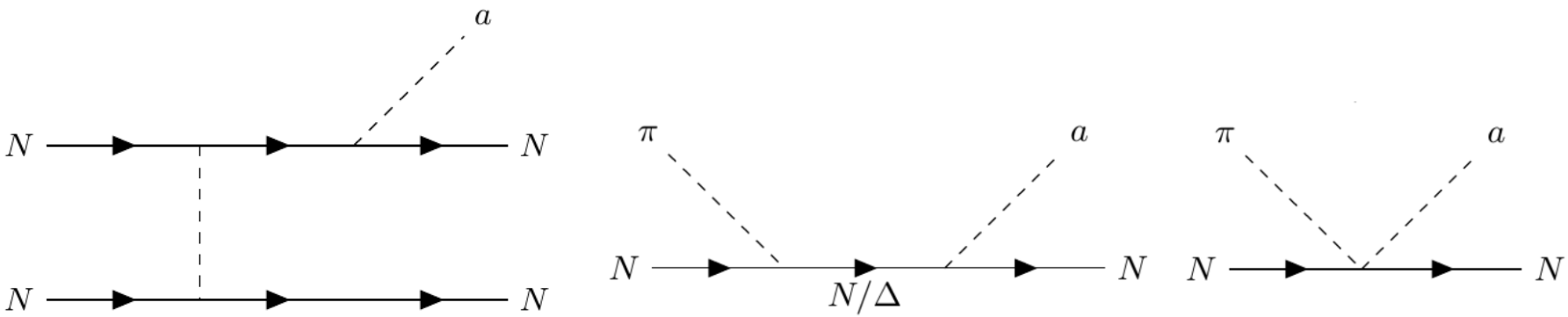

ALP production spectrum (number density of ALPs produced per unit time and energy)

$$\frac{d^2 n_a}{dE_a dt} = \prod_i \int \frac{g_i d^3\vec{p}_i}{(2\pi)^3 2E_i} f_i(E_i) \prod_{j\neq a} \int \frac{d^3\vec{p}'_j}{(2\pi)^3 2E'_j} [1-f_j(E'_j)]\,(2\pi)^4 \delta^4\left(\sum_i p_i - \sum_{j\neq a} p'_j - p_a\right) \frac{|\vec{p}_a|}{4\pi^2} |\overline{\mathcal{M}}|^2$$

Fermi-Dirac distribution function for nucleons $f(E_N) = \frac{1}{1-\exp\left(\frac{E_N-\mu_N}{T}\right)}$, Bose-Einstein distribution function for pions $f(E_\pi) = \frac{1}{1+\exp\left(\frac{E_\pi-\mu_\pi}{T}\right)}$, nucleon and pion chemical potentials μ_N and μ_π

Axion spectrum at Earth from one SN

The spectral fluence of ALPs from an isotropic production spectrum far away from the SN

$$\frac{dN_a}{dE_a^{*\infty}} = \int_{t_{\rm min}}^{t_{\rm max}} dt \int_0^\infty \alpha(r)^{-1} 4\pi r^2 dr \left\langle e^{-\tau(E_a^*, r)} \right\rangle \frac{d^2 n_a}{dE_a dt} \left(r, t, \alpha(r)^{-1} E_a^{*\infty}\right),$$

$E_a^{*\infty} = \alpha(r) E_a$ the observed energy at infinity,

$\alpha(r) \leq 1$ the lapse factor accounting for the gravitational redshift inside and outside the star

Absorption effects from $N + N + a \to N + N$ and $N + a \to N + \pi$

$$\left\langle e^{-\tau(E_a^*, r)} \right\rangle = \frac{1}{2} \int_{-1}^{+1} d\mu \, e^{-\int_0^\infty ds \, \Gamma_a \left(E_a^*, \sqrt{r^2 + s^2 + 2rs\mu}\right)}$$

$E_a^* = \frac{\alpha(r)}{\alpha\left(\sqrt{r^2+s^2+2rs\mu}\right)} E_a$ redshifted from the point of ALP production to the point of absorption

The absorption rate

$$\Gamma_a \left(E_a, r\right) = \lambda_a^{-1} \left(E_a, r\right) \left[1 - e^{-\frac{E_a}{T(r)}}\right],$$

$\lambda_a \left(E_a, r\right)$ the ALP mean free path

Diffuse galactic SN ALP flux at Earth

- SN MeV ALPs travel with semi-relativistic velocities due to their massive nature
- ALPs are produced with $E_a = [m_a - \mathcal{O}(100)\,\mathrm{MeV}] \Rightarrow$ spread in arrival time Δt

  For a SN at the Galactic Center and $m_a \simeq 1 - 100$ MeV, $\Delta t \sim 5 \times 10^2 - 5 \times 10^3$ yrs

  Galactic SN rate ~ 1.63 per century *Rozwadowska et al. New Astron 83 (2021)* $\Rightarrow$
  $\sim 10 - 100$ SN ALP fluxes overlap at Earth $\Rightarrow$ near constant diffuse ALP flux

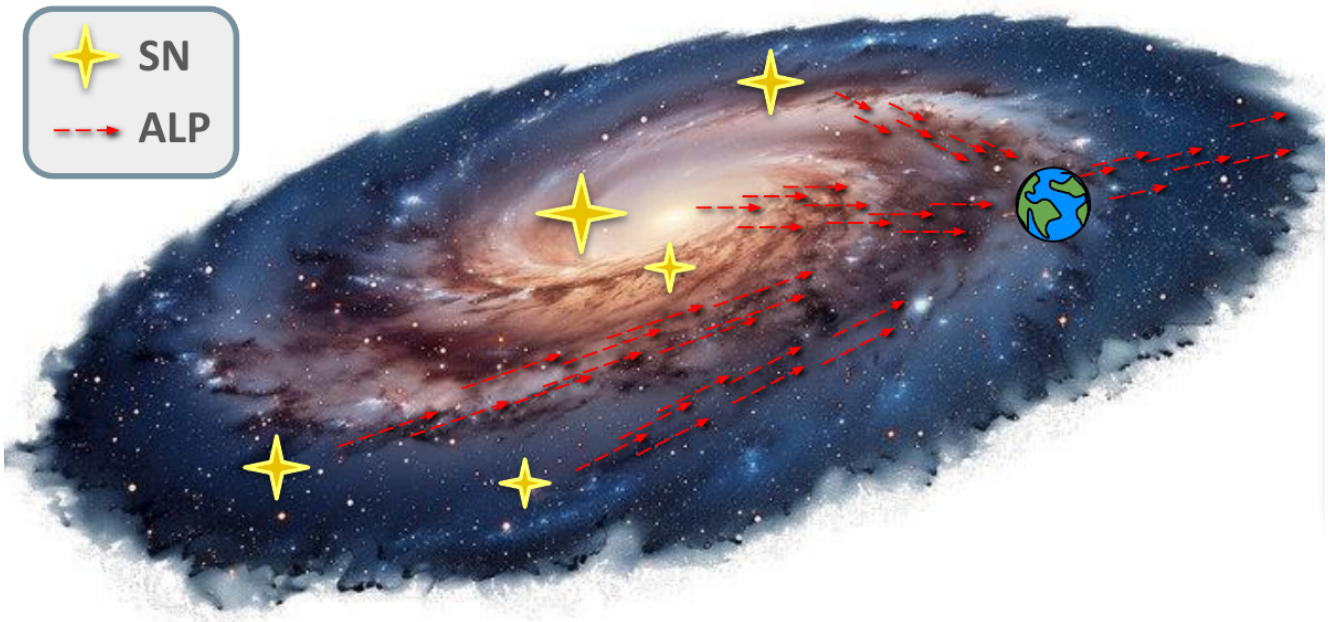

Diffuse galactic SN ALP flux at Earth

The galactic SN rate *Adams et al., ApJ 778 (2013) 164, McMillan MNRAS 466 (2017)*

$$\frac{dn_{SN}}{dt} = A\, \mathrm{e}^{-\frac{r}{R_d}}\, \mathrm{e}^{-\frac{|z|}{H}}$$

For ccSNe:

$R_d \simeq 2.6$ kpc H=0.3kpc

SN rate: 1.63 per century

A = 1.65 x 10^{-3} kpc^{-3} yr^{-1}

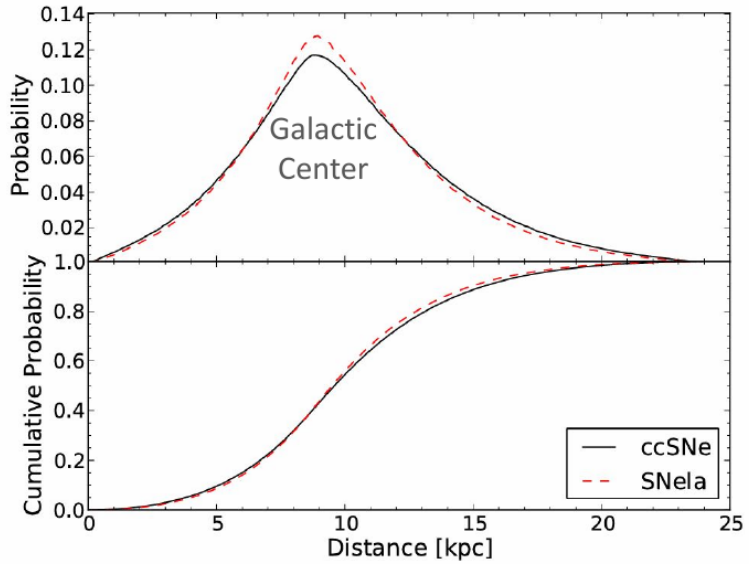

The total ALP spectrum from galactic SN that reaches Earth ($E_a^{\mathrm{Earth}} \equiv E_a^{*\infty}$)

$$\frac{d\Phi_a}{dE_a^{\mathrm{Earth}}} = \frac{dN_a}{dE_a^{\mathrm{Earth}}} \int_{-\infty}^{\infty} \int_0^{2\pi} \int_0^{\infty} \frac{dn_{SN}}{dt}\, \frac{r}{4\pi\,(\vec{r} - \vec{R}_E)^2}\, dr\, d\theta\, dz\,,$$

$|\vec{R_E}| = 8.23$ kpc Earth-GC distance and $z_E = 20.8$ pc its position above the mid-plane of the disk

Diffuse galactic SN ALP flux at Earth

$$\frac{d\Phi_a}{dE_a^{\rm Earth}} = 1.3 \times 10^{-55}\ {\rm cm}^{-2}\ {\rm s}^{-1}\ \frac{dN_a}{dE_a^{\rm Earth}}$$

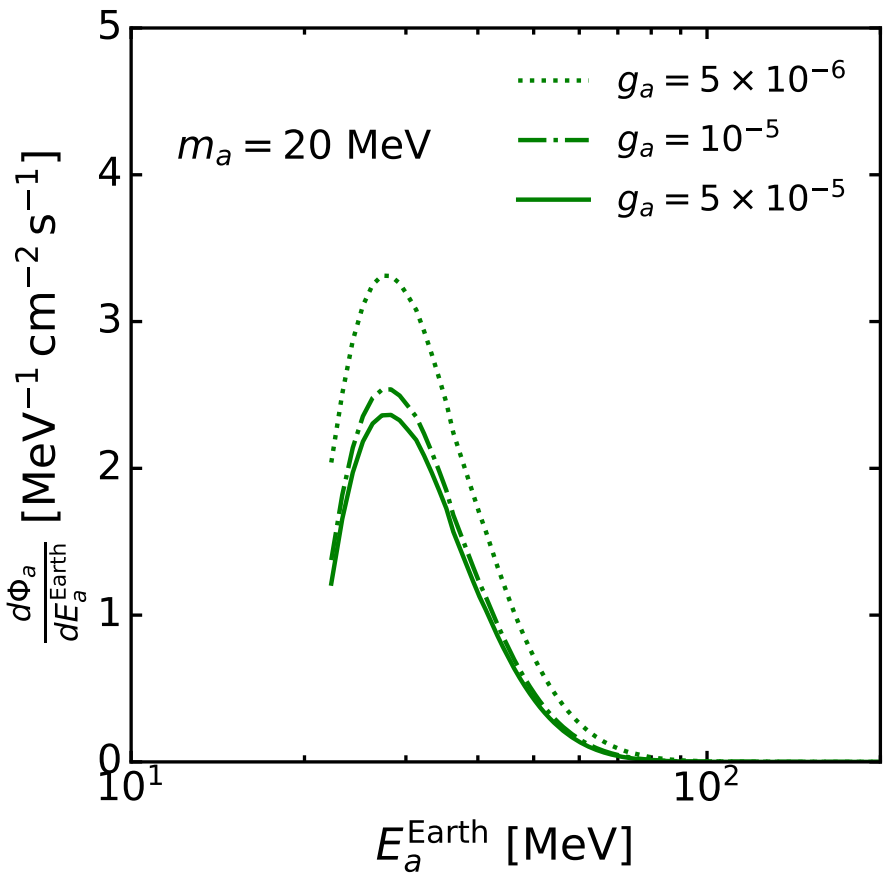

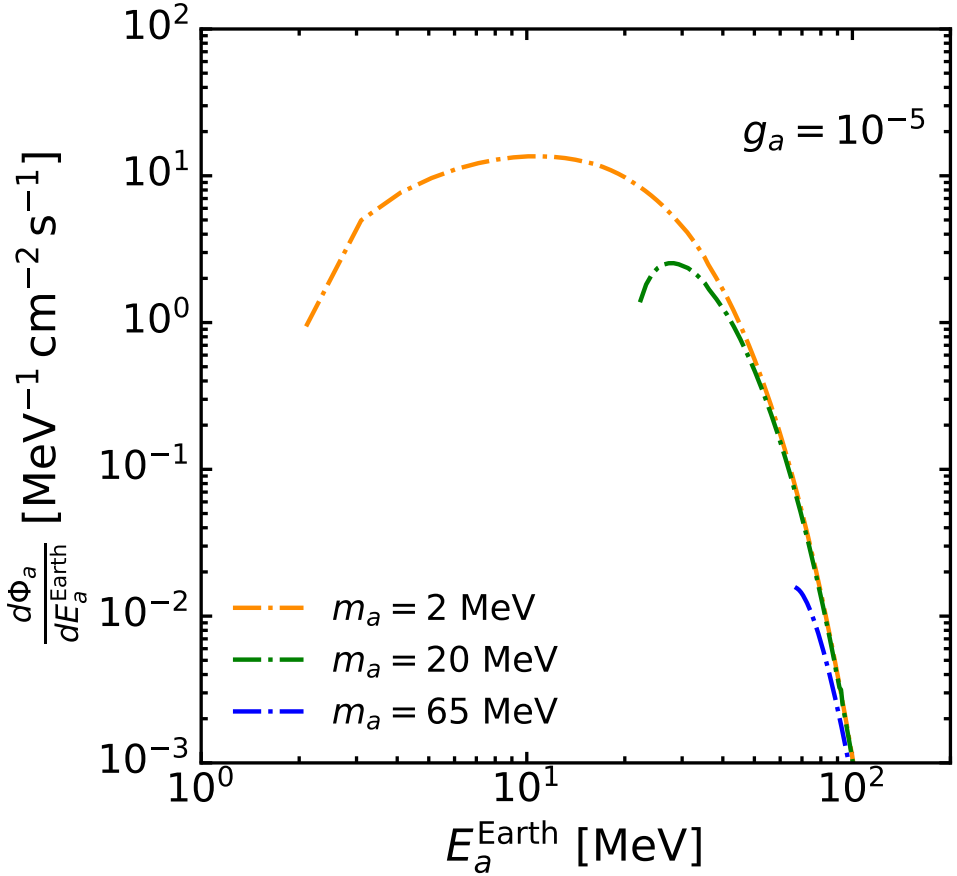

Detection of diffuse SN ALPs in neutrino detectors

ALPs reach neutrino detectors and produce MeV photons after interacting on free protons

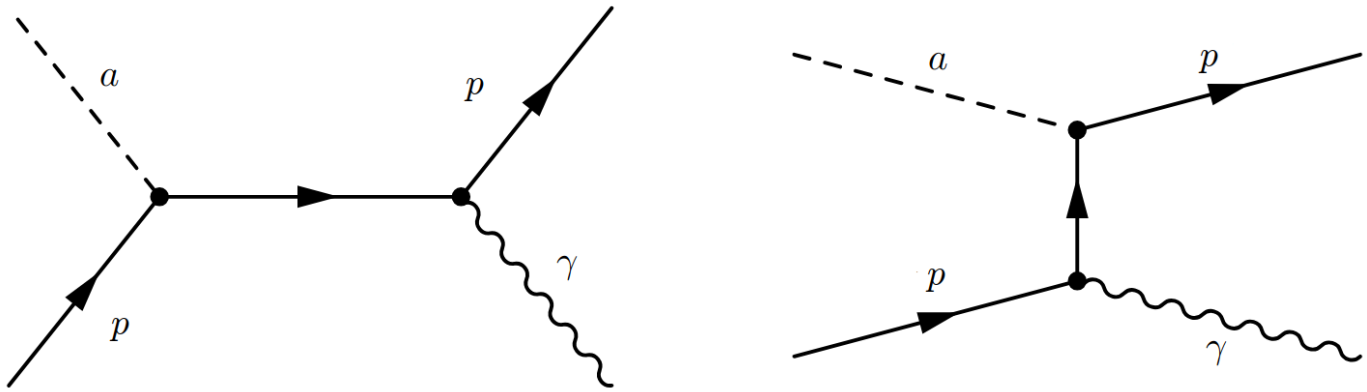

Number of photons per energy and time produced at an experiment with N_t targets

$$\frac{d\,N_\gamma}{dE_\gamma} = N_t \int_{E_a^{min}(E_\gamma)}^{E_a^{max}(E_\gamma)} dE_a^{\rm Earth} \frac{d\Phi_a}{dE_a^{\rm Earth}} \frac{d\,\sigma_{ap\to p\gamma}}{d\,E_\gamma}$$

$E_a^{max}(E_\gamma) \sim E_a^{min}(E_\gamma) \sim E_\gamma$, for $1\,\text{MeV} < E_a < 100\,\text{MeV}$ ($10^{-3}\,\text{MeV} < E_\gamma^{\rm max} - E_\gamma^{\rm min} < 18$ MeV)

Signal never explored before, expected in any model with ALP-proton coupling

Events in Super-Kamiokande

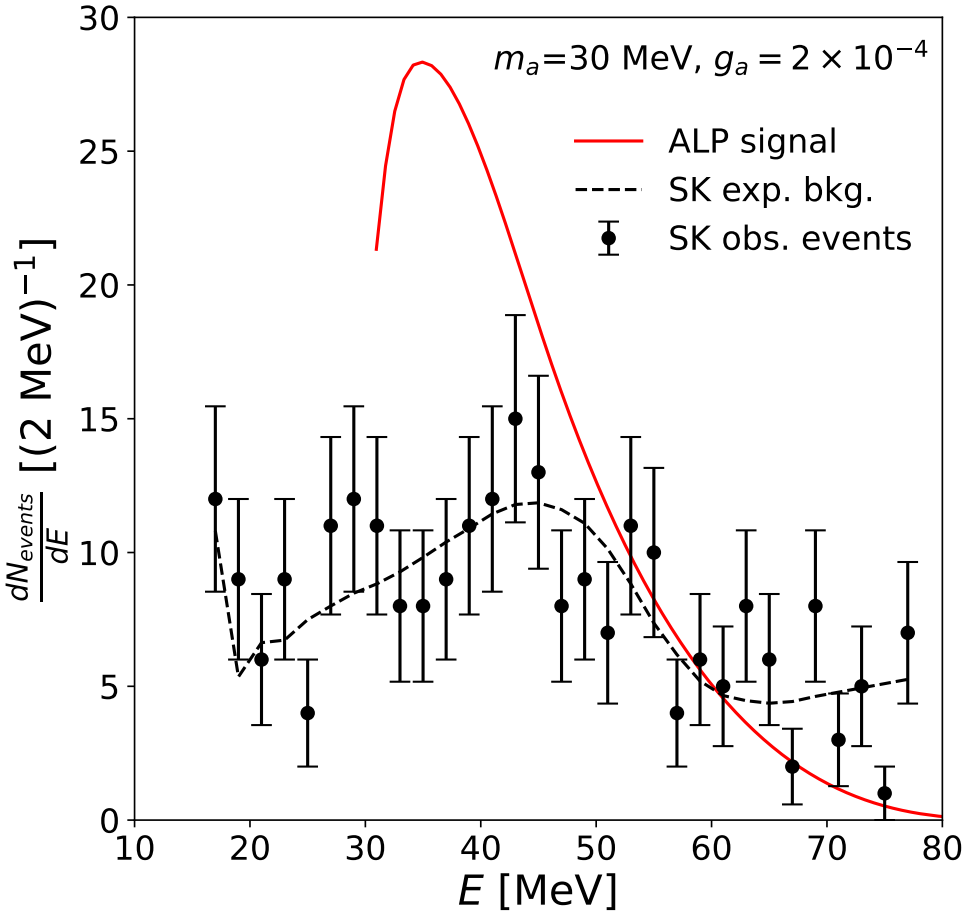

- Super-Kamiokande (SK) phase IV, exposure 22.5×2970-kton·day
- Energy region $E = 16 - 80$ MeV optimized to search for the DSNB by identifying positrons from inverse beta decay, without neutron coincidence
- Background dominated by cosmic ray muon spallation, electrons produced by the decays of low energy muons and pions, and charged current interactions of atmospheric neutrinos

Bounds from SK and projections for HK

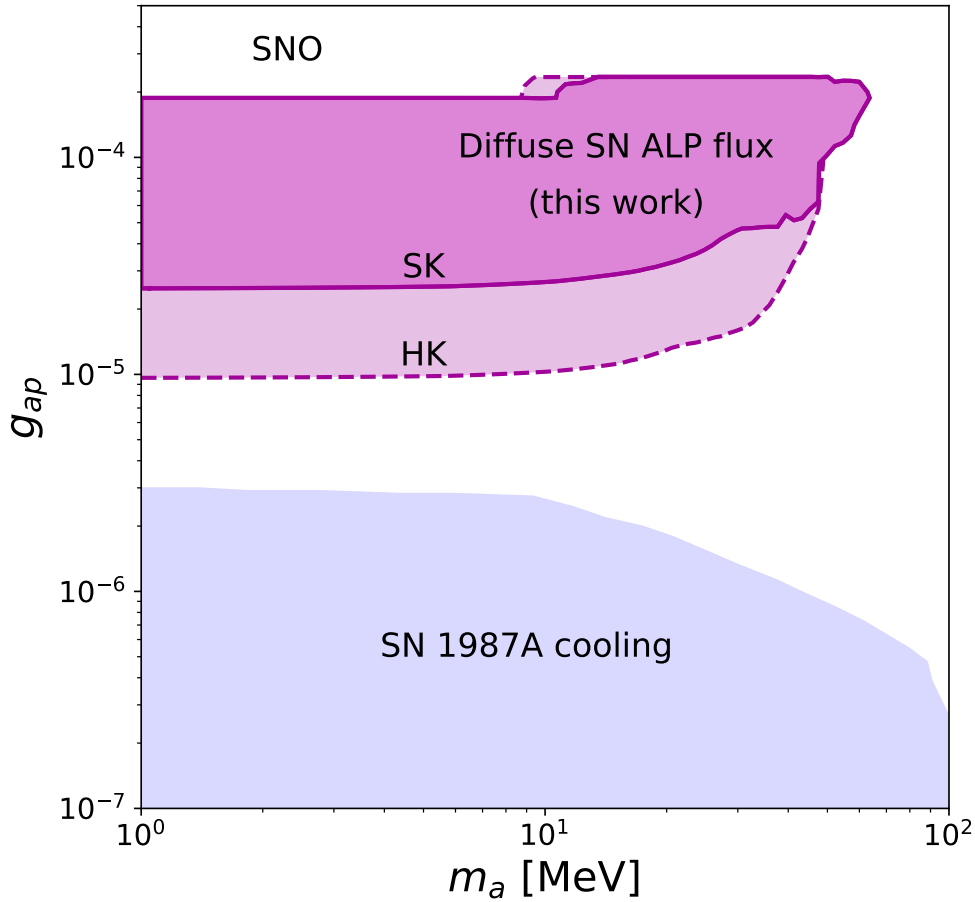

- No observation of anomalous events in SK ⇒ constraints on the ALP-proton coupling

  Binned analysis with 2 MeV bin width
  Considering all SK exposure, but dominated by phase IV

- Projections for Hyper-Kamiokande (HK), exposure 187×10 kton yrs
  Background from the HK report, limited to [16-50] MeV

Conclusions

- ALPs with masses $\sim 1 - 200$ MeV can be produced in core collapse SN due to their coupling to nucleons and constitute a galactic diffuse background
- MeV-ALPs will reach neutrino detectors and will produce MeV-photons via $a\,p \to p\,\gamma$, which can be detected with very small background
- Current neutrino water Cherenkov detectors exclude ALPs with $1\,\mathrm{MeV} \lesssim m_a \lesssim 70\,\mathrm{MeV}$ and couplings $g_{ap} \sim 2 \times 10^{-5} - 2 \times 10^{-4}$ for the KSVZ model
- Future water Cherenkov detectors could go a factor ~ 2 lower in couplings

Backup slides

SN profiles

Ferreira, Marsh, Müller, JCAP 11 (2022) 057

$t = 1$ s post-bounce

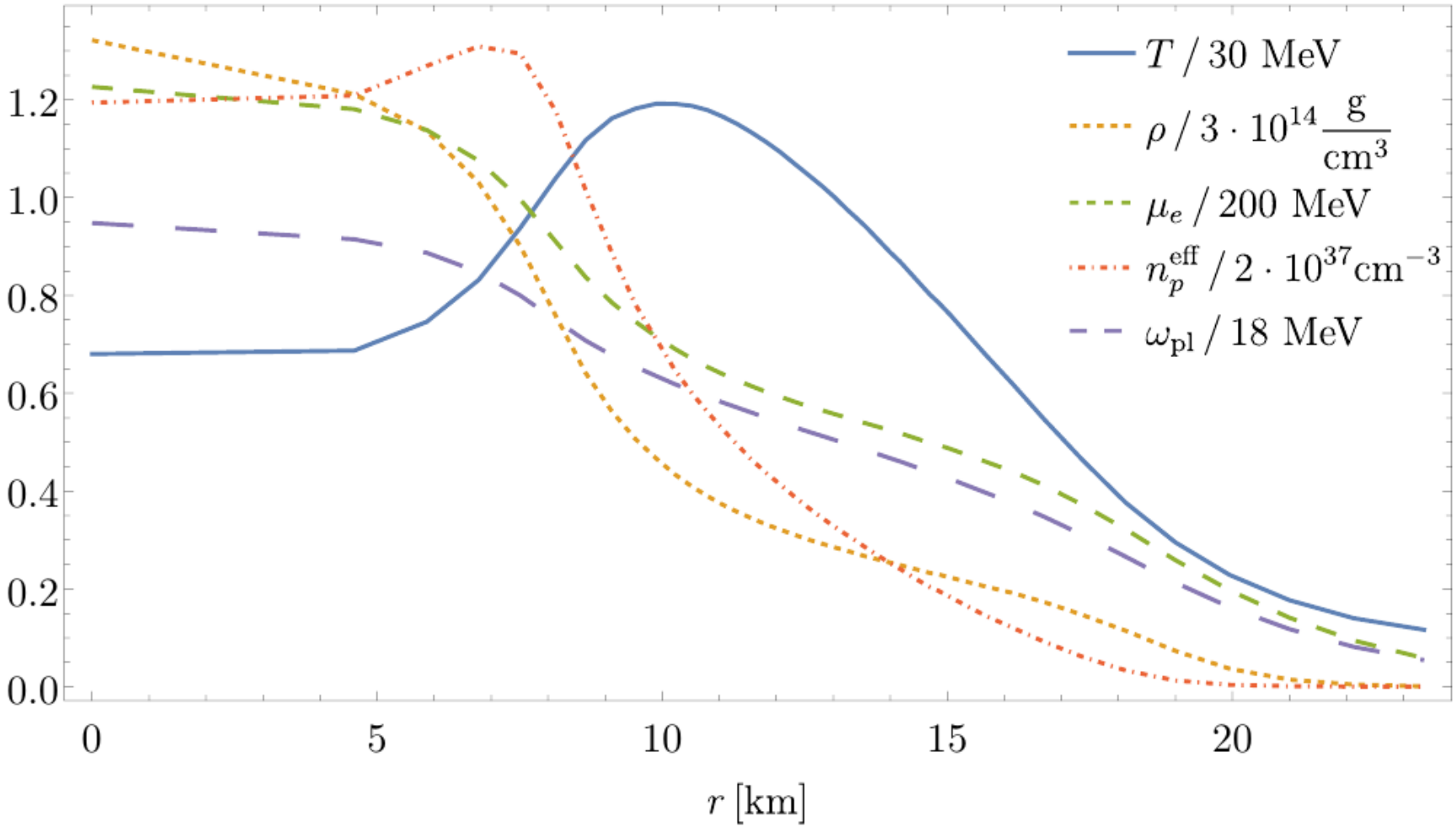

Effect of ALPs on the profiles

Fischer et al., PRD 104 (2021) 103012

$t = 1$ s post-bounce

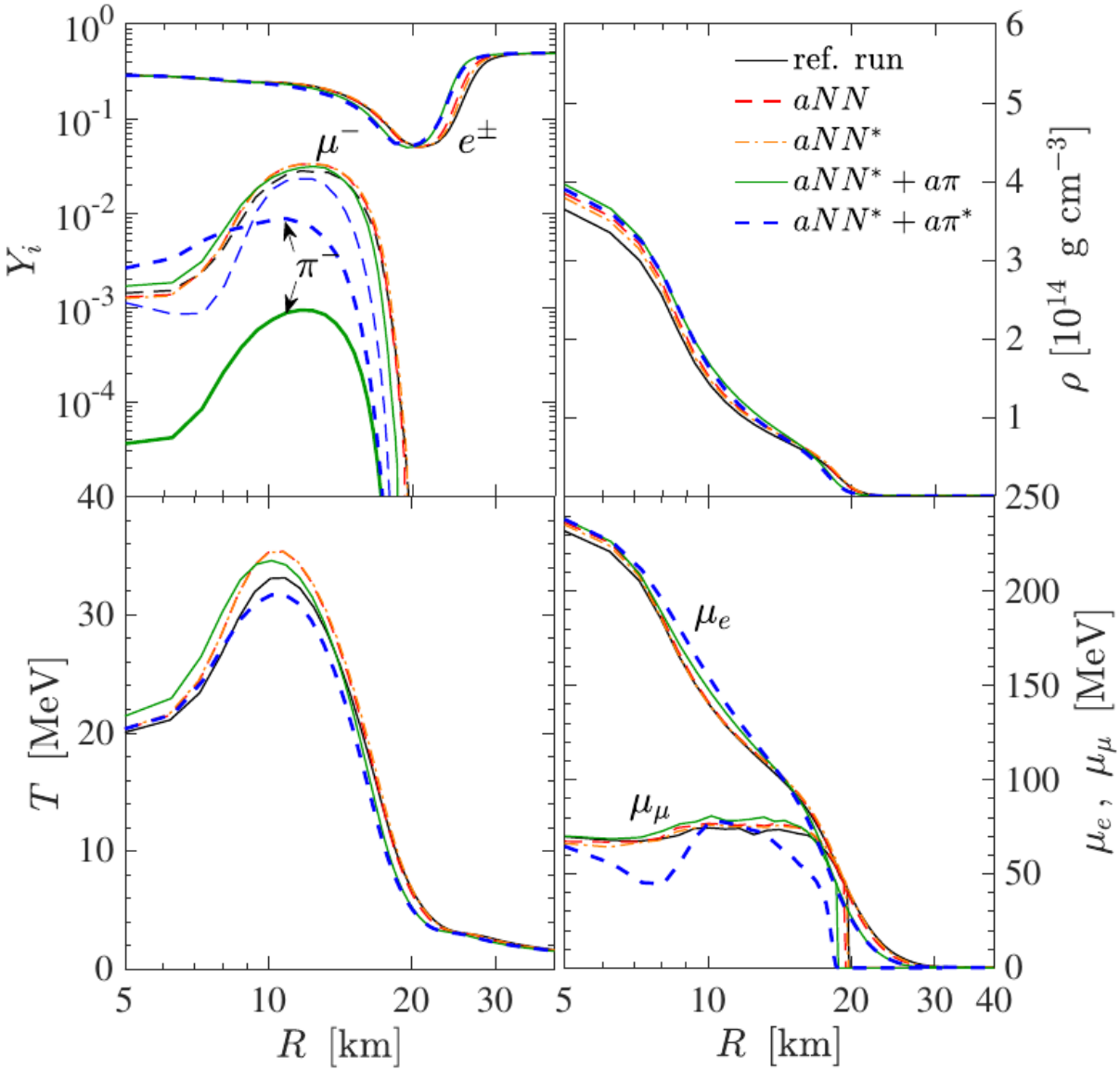

Effect of ALPs on the profiles

Fischer et al., PRD 104 (2021) 103012

$t = 7$ s post-bounce

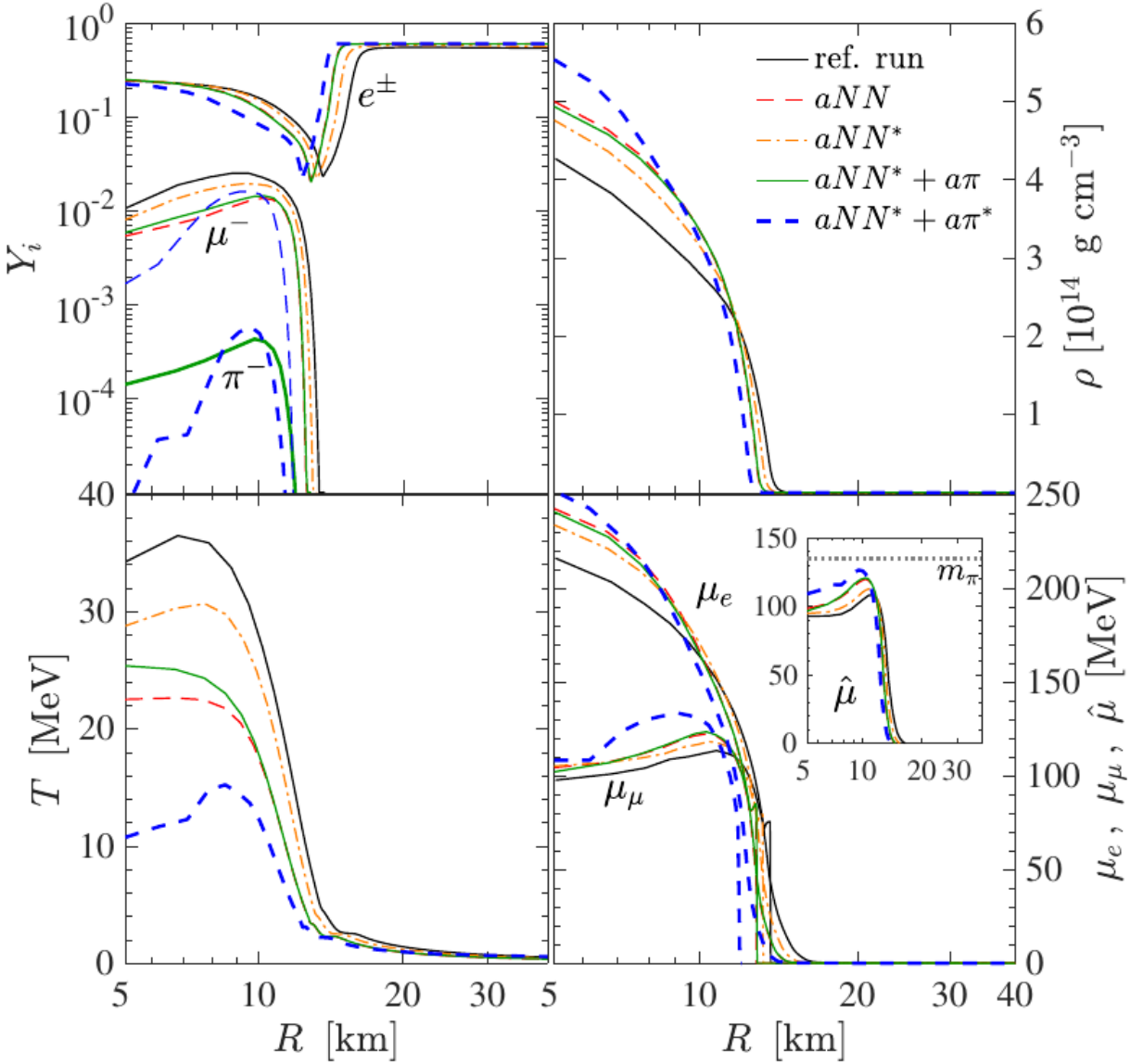

Cumulative percentage of SN vs progenitor star mass

Sukhbold et al., ApJ. 821 (2016) 38

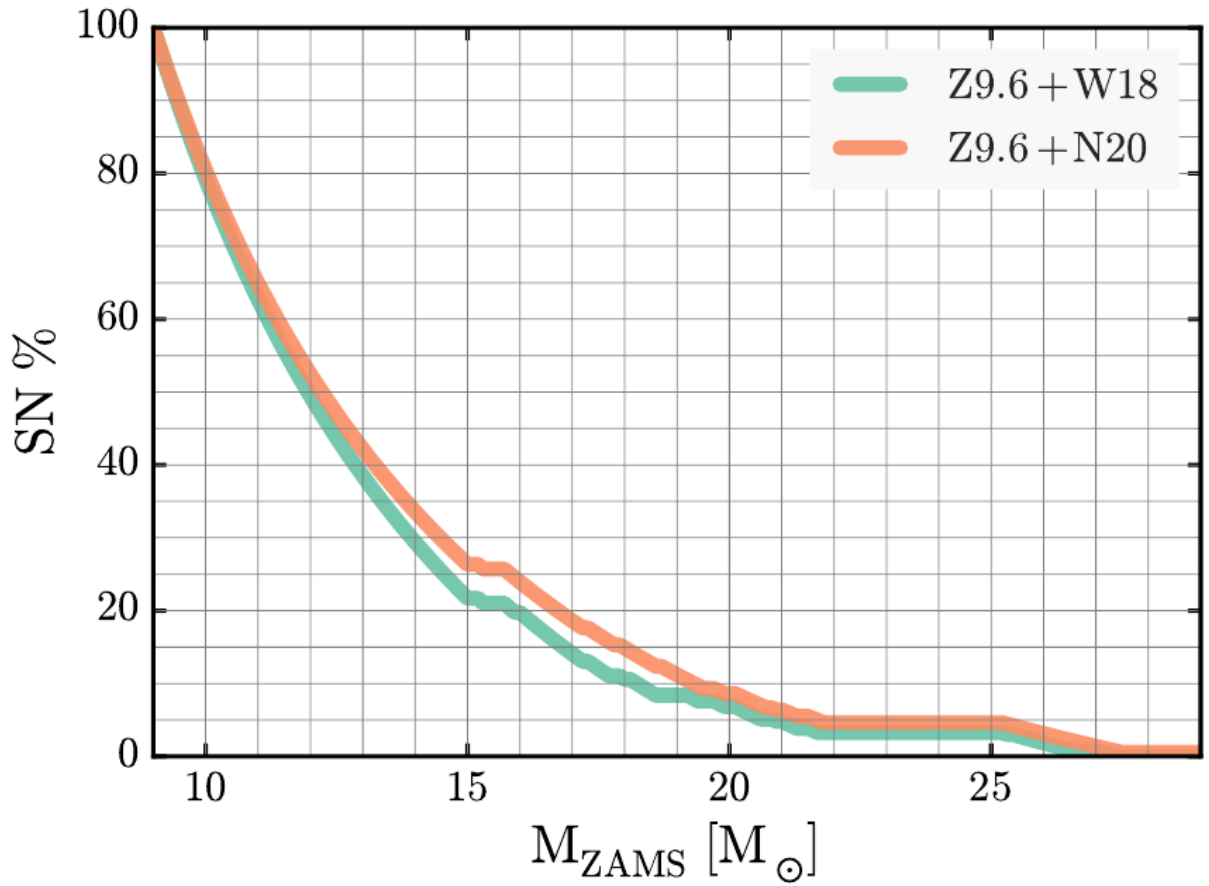

FIG. 14.— The percentage of Type II supernovae above a given main sequence mass for explosions using the Z9.6 and W18 or N20 engines. A Salpeter IMF has been assumed. Successful explosions above 30 $M_\odot$ do not make Type II supernovae.

SN profiles for different progenitor masses

Calore et al., PRD 105 (2022) 063028

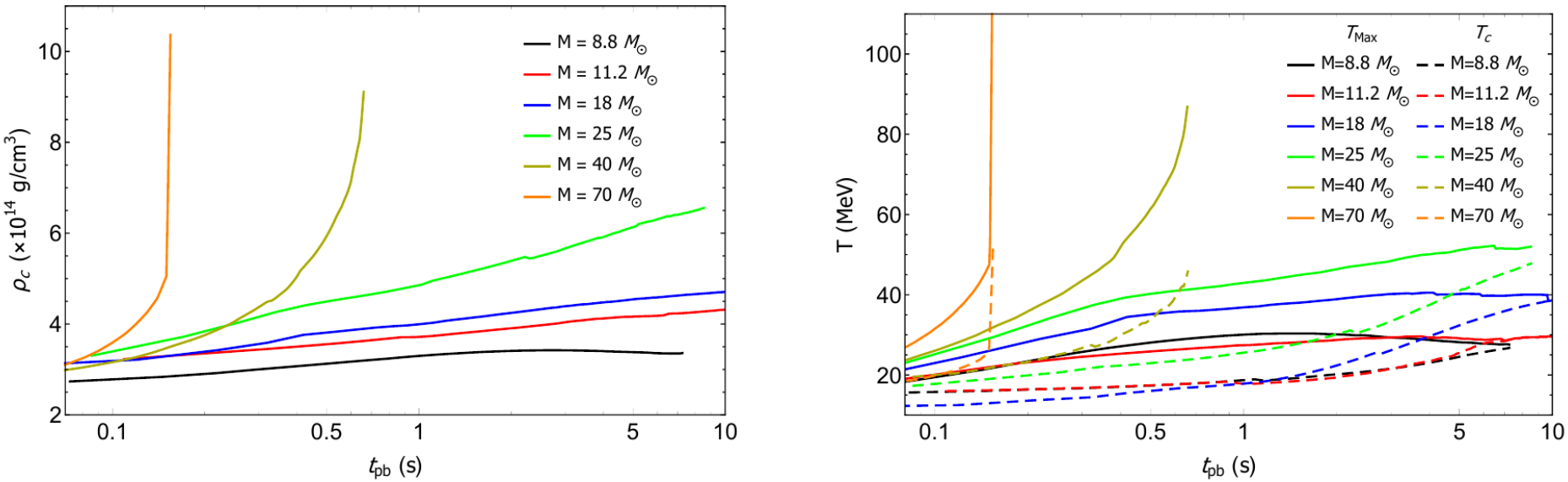

FIG. 1. PNS evolution during the deleptonization phase for the SN explosion models launched from different progenitors with ZAMS masses of 8.8, 11.2, 18.0 and 25 $M_\odot$. *Left panel*: central density, $\rho_{\rm centre}$. *Right panel*: central and maximum temperatures, $T_{\rm centre}$ (dashed lines) and $T_{\rm Max}$ (solid lines).

QCD ALPS

The lagrangian for QCD ALPs with interactions to quarks and gluons

$$\mathcal{L}_{a\text{QCD}} = c_g \frac{g_s^2}{32\pi^2}\frac{a}{f_a} G^a_{\mu\nu}\tilde{G}^{a\mu\nu} + \sum_q c_q \frac{\partial_\mu a}{2f_a}\bar{q}\gamma^\mu\gamma_5 q + \frac{(m_{a,0})^2}{2}a^2$$

$f_a = \frac{m_N}{g_a}$, $G^a_{\mu\nu}$ the gluon field strength tensor, $\tilde{G}^a_{\mu\nu} = \frac{1}{2}\epsilon_{\mu\nu\rho\sigma}G^{a\rho\sigma}$ its dual, c_g and c_q model-dependent constants, with $q = u, d, s, c, t, b$

Below the QCD confinement scale $\mathcal{L}_{a\text{QCD}}$ induces ALP couplings with baryons and mesons.
The nuclear interaction Lagrangian derived in the context of Heavy Baryon Chiral Perturbation Theory

$$\mathcal{L}_{\text{nuc}} = \frac{\partial^\mu a}{2f_a}\left[C_p\bar{p}\gamma^\mu\gamma_5 p + C_n\bar{n}\gamma^\mu\gamma_5 n + \frac{C_{a\pi N}}{f_\pi}\left(i\pi^+\bar{p}\gamma^\mu n - i\pi^-\bar{n}\gamma^\mu p\right) + C_{aN\Delta}\left(\bar{p}\Delta^+_\mu + \bar{\Delta}^+_\mu p + \bar{n}\Delta^0_\mu + \bar{\Delta}^0_\mu n\right)\right]$$

$$C_{a\pi N} = \frac{\left(C_p - C_n\right)}{\sqrt{2}g_A}, \quad C_{aN\Delta} = -\frac{\sqrt{3}}{2}\left(C_p - C_n\right),$$

$f_\pi = 92.4\text{MeV}$, $g_A = 1.28$,

$$\begin{aligned} C_p\left(c_g, c_u, c_d\right) = &-0.47c_g + 0.88c_u - 0.39c_d - 0.038c_s \\ &- 0.012c_c - 0.009c_b - 0.0035c_t \\ C_n\left(c_g, c_u, c_d\right) = &-0.02c_g + 0.88c_d - 0.39c_u - 0.038c_s \\ &- 0.012c_c - 0.009c_b - 0.0035c_t \end{aligned}$$

Nucleon electric-dipole portal for QCD-ALPs

The gluonic part of the lagrangian

$$\mathcal{L}_{ag} = c_g \frac{g_s^2}{32\pi^2} \frac{a}{f_a} G^a_{\mu\nu} \tilde{G}^{a\mu\nu}$$

induces a model independent nucleon EDM portal interaction *Pospelov, Ritz, PRL 83 (1999) 2526*

$$\mathcal{L}_a^{\text{nEDM}} = -\frac{i}{2} g_{d,N} a \bar{N} \gamma_5 \sigma_{\mu\nu} N F^{\mu\nu}$$

with $g_{d,N} = \frac{C_{aN\gamma}}{m_N f_a}$, with $f_a = \frac{m_N}{g_a}$ and $C_{an\gamma} = -C_{ap\gamma} = 0.0033(15)$

ALP production in SN: bremsstrahlung

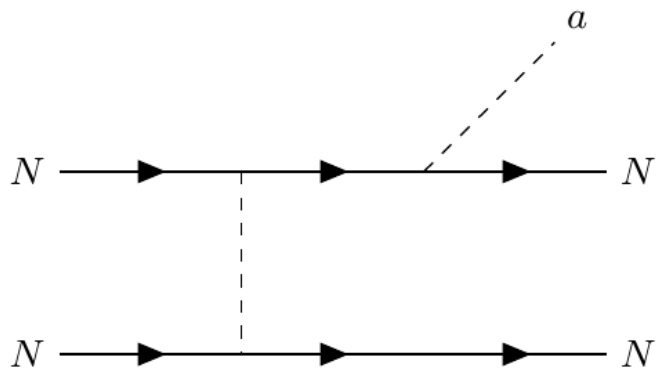

Axion emission spectrum *Giannotti, Nesti, PRD 72 (2005) 063005*

$$\left(\frac{d^2 n_a}{dE_a dt}\right)_{NN} = \frac{g_a^2}{16\pi^2}\frac{n_B}{m_N^2}\left(E_a^2 - m_a^2\right)^{\frac{3}{2}} e^{-\frac{E_a}{T}} S_\sigma\left(E_a\right)\Theta\left(E_a - m_a\right),$$

nucleon structure function $S_\sigma\left(E_a\right) = \frac{\Gamma_\sigma}{E_a^2+\Gamma^2} s\left(\frac{E_a}{T}\right)$, $s\left(\frac{E_a}{T}\right)$ dimensionless nuclear function

nucleon spin fluctuation rate $\Gamma_\sigma = 4\pi^{-1.5}\left(\frac{g_A}{2f_\pi}\right)^4 T^{0.5} m_N^{0.5}\rho$, $\Gamma = g\Gamma_\sigma$,
g from scattering kernel normalization

ALP production in SN: pion-axion conversion

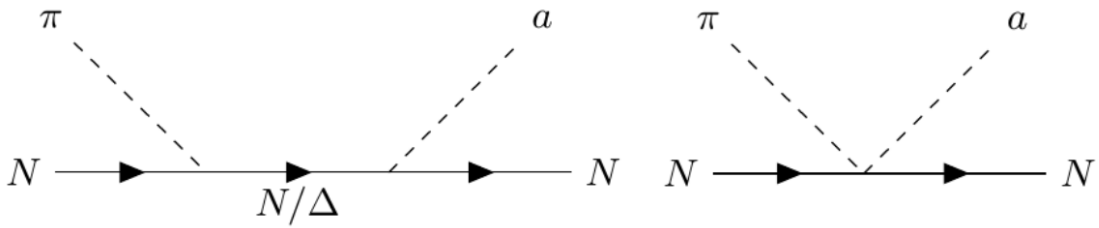

Axion emission spectrum *Carenza et al., PRL 126 (2021) 071102*

$$\left(\frac{d^2 n_a}{dE_a dt}\right)_{N\pi} = \frac{g_a^2 T^{1.5}}{2^{1.5}\pi^5 m_N^{0.5}} \left(\frac{g_A}{2f_\pi}\right)^2 \left(E_a^2 - m_a^2\right)^{\frac{1}{2}}$$
$$\times C_a^{p\pi^-} \frac{\Theta\left(E_a - \max\left(m_a, m_\pi\right)\right)}{\exp\left(x_a - y_\pi - \hat{\mu}_\pi\right) - 1} \left(E_a^2 - m_\pi^2\right)^{\frac{1}{2}} \frac{E_a^2}{E_a^2 + \Gamma^2}$$
$$\times \int_0^\infty dy y^2 \frac{1}{\exp\left(y^2 - \hat{\mu}_p\right) + 1} \frac{1}{\exp\left(-y^2 + \hat{\mu}_n\right) + 1}$$

$C_a^{p\pi^-} = \frac{m_N^2}{g_A^2}\beta_a^2 \mathcal{G}_a\left(|\mathbf{p}_\pi|\right)$ term related to the matrix element with $\mathcal{G}_a\left(|\mathbf{p}_\pi|\right)$ a dimensionless function

$\hat{\mu}_i = \frac{\mu_i - m_i - U_i}{T}$ the degeneracy parameter with μ_i and U_i the chemical potential and the self-energies of the particles, $y_\pi = m_\pi/T$, $x_a = E_a/T$

ALP photo-production in SN

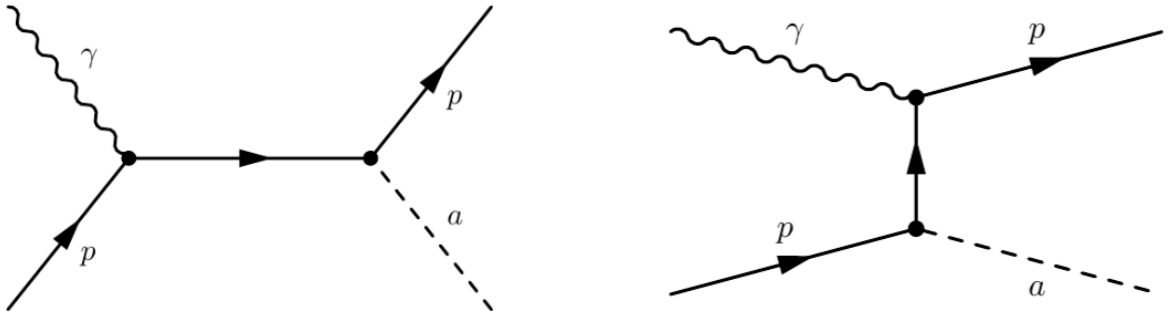

Axion emission spectrum

$$\left(\frac{d^2 n_a}{dE_a dt}\right)_{p\gamma} = n_p^{\text{eff}} \frac{6}{(2\pi)^2} \int dE_\gamma \frac{1}{e^{E_\gamma/T} - 1} (E_\gamma^2 - m_\gamma^2) \frac{d\sigma_{\gamma p \to p\, a}}{dE_a}$$

$n_p^{\text{eff}} \equiv 2 \int \frac{d^3\vec{p}}{(2\pi)^3} f_p(E)(1 - f_p(E))$ effective number density of protons,

f_p the Fermi-Dirac distribution function

m_γ effective photon mass

Differential cross section for ALP photo-production in SN

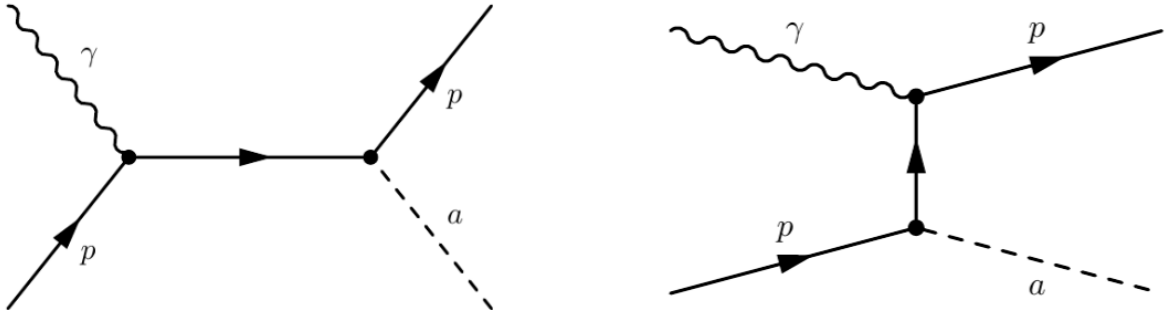

$$\frac{d\sigma_{\gamma p\to p\,a}}{dE_a} = \frac{1}{32\pi}\int_{-1}^{1}\frac{\left|\overline{\mathcal{M}}\right|^2}{\left|\vec{p_\gamma}\right|^2 m_p^*}\,\delta(\cos\theta_a - \cos\theta_a^0)\,d\cos\theta_a$$

with

$$\cos\theta_a^0 = \frac{E_\gamma E_a - m_p^*(E_\gamma - E_a) - \frac{1}{2}(m_a^2 + m_\gamma^2)}{\sqrt{E_\gamma^2 - m_\gamma^2}\,\sqrt{E_a^2 - m_a^2}} \tag{1}$$

determined by energy conservation, and with the averaged squared amplitude given by

$$\left|\overline{\mathcal{M}}\right|^2 = \frac{4}{3}C_{ap}^2 e^2 g_a^2 m_p^*\left[\frac{2E_a(m_a^2 + E_\gamma m_p^*) + m_a^2(m_p^* - E_\gamma) - 4E_a^2 m_p^* + E_a m_\gamma^2}{(m_a^2 - 2E_a m_p^*)^2}\right.$$
$$\left. + \frac{m_a^2(m_p^* - E_\gamma)}{(2E_\gamma m_p^* + m_\gamma^2)^2} + \frac{2m_a^2 m_p^* - 2E_a^2 m_p^* - E_a m_a^2}{(m_a^2 - 2E_a m_p^*)(2E_\gamma m_p^* + m_\gamma^2)}\right]. \tag{2}$$

ALP production in SN: comparison

$R = 10$ km, $m_a = 20$ MeV, $g_a = 10^{-5}$

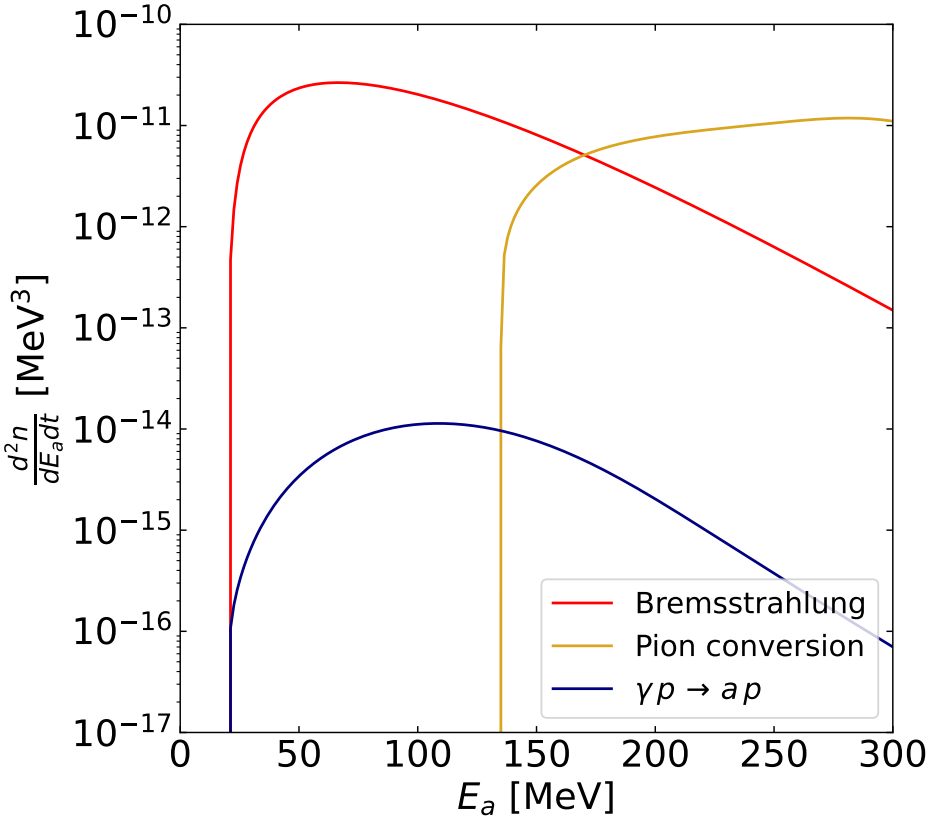

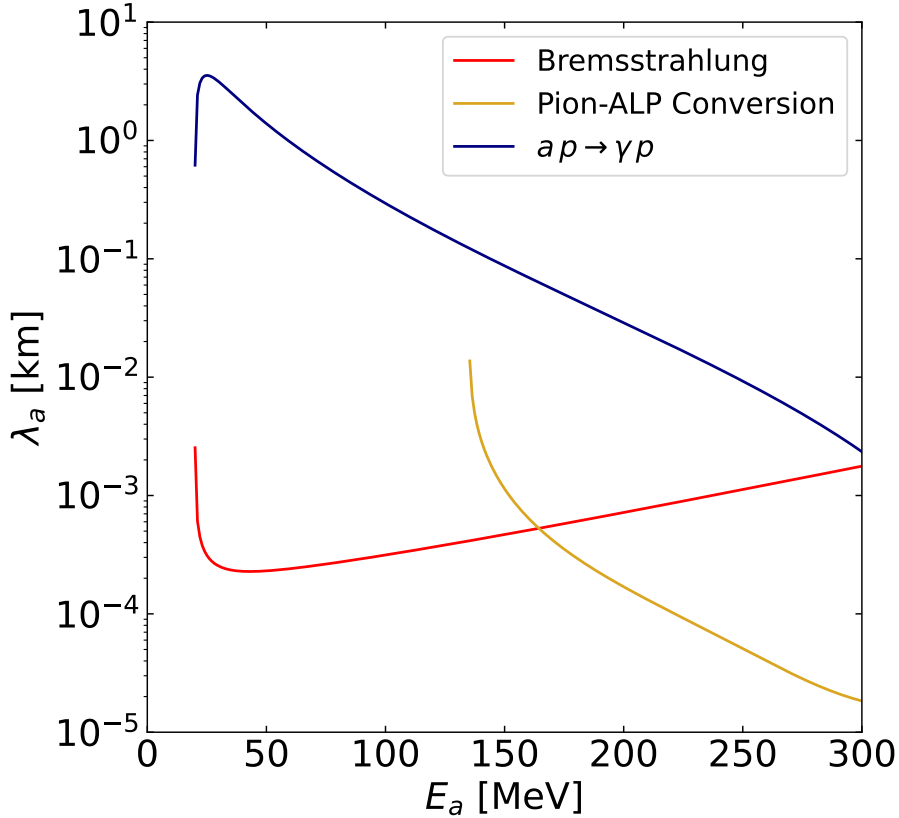

Negligible ALP photo-production, no absorption via $a\,p \to \gamma\,p$

ALP production in SN: comparison

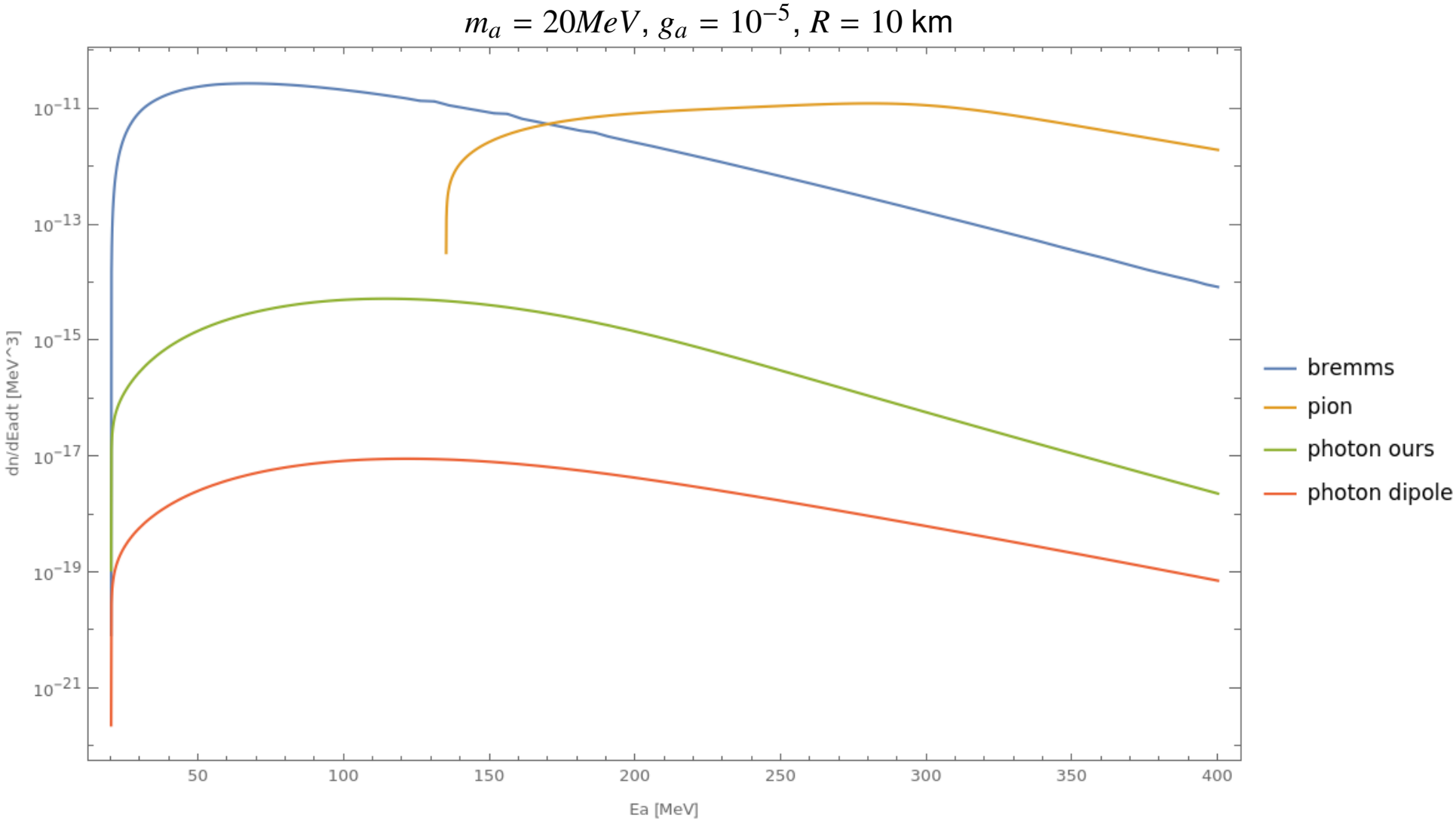

Lapse function

The lapse function encodes effects due to the proto-NS gravitational potential $\Phi(r)$ evaluated locally in the proto-NS interior

$$\alpha(r) = \sqrt{1 - 2\Delta\Phi(r)}$$

$\Delta\Phi(r) = G\int_r^\infty \frac{m_{\rm enc}(r')}{r'^2} dr'$ change in potential from r to ∞ and $m_{\rm enc}(r')$ mass enclosed in r'

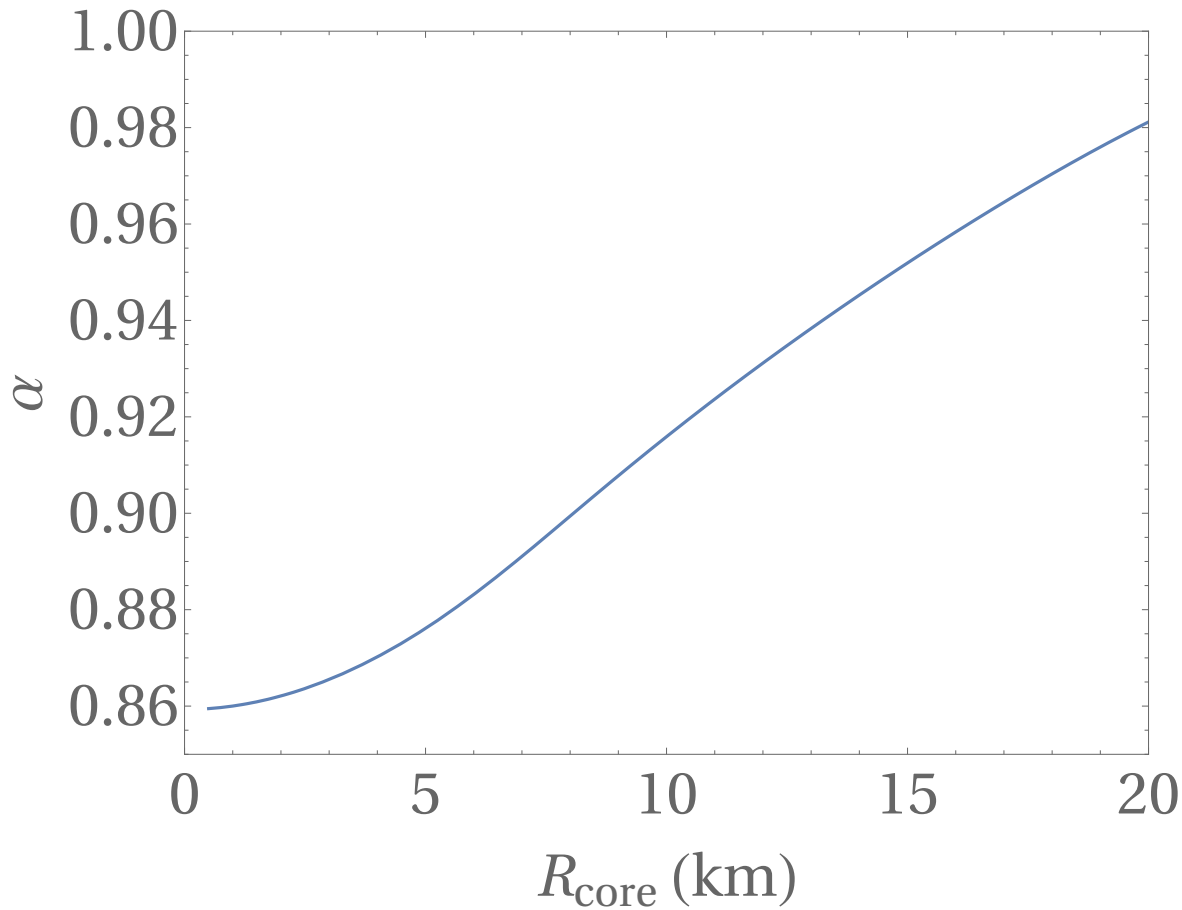

ALP spectrum at Earth for other models

$m_a = 10$ MeV, $g_a = 10^{-6}$

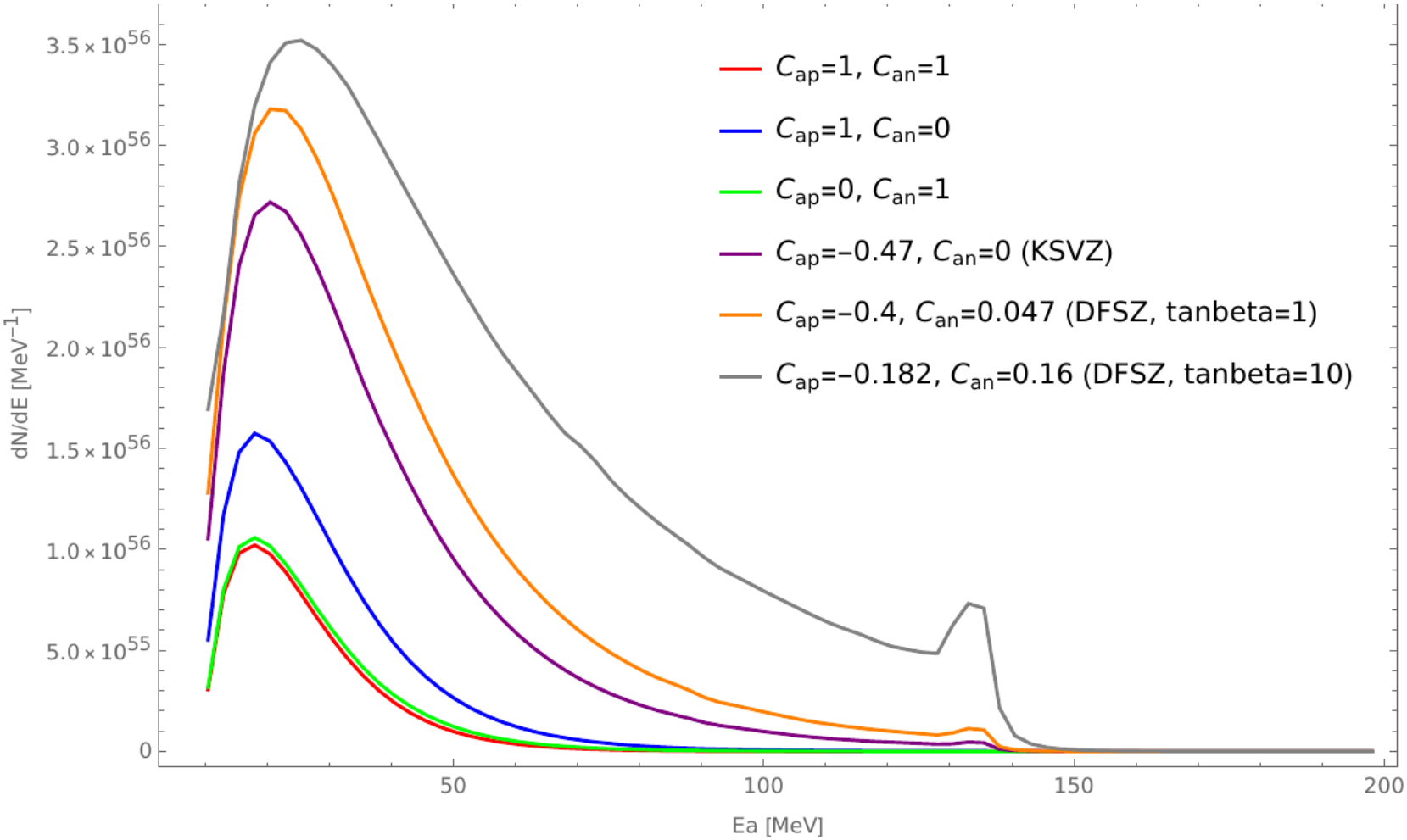

Mean-free path

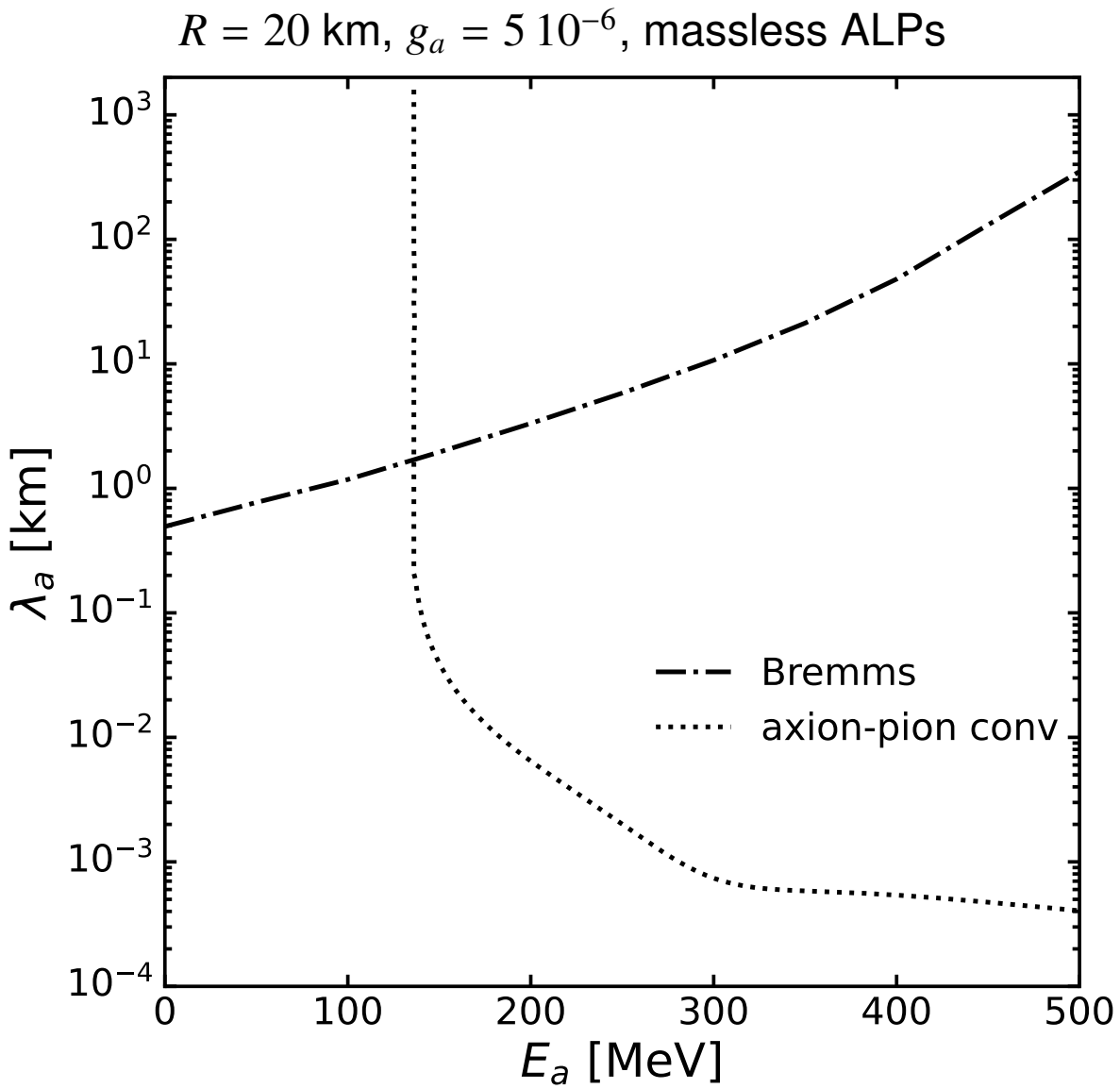

Mean-free path

$R = 20$ km, $g_a = 5\,10^{-6}$, massless ALPs

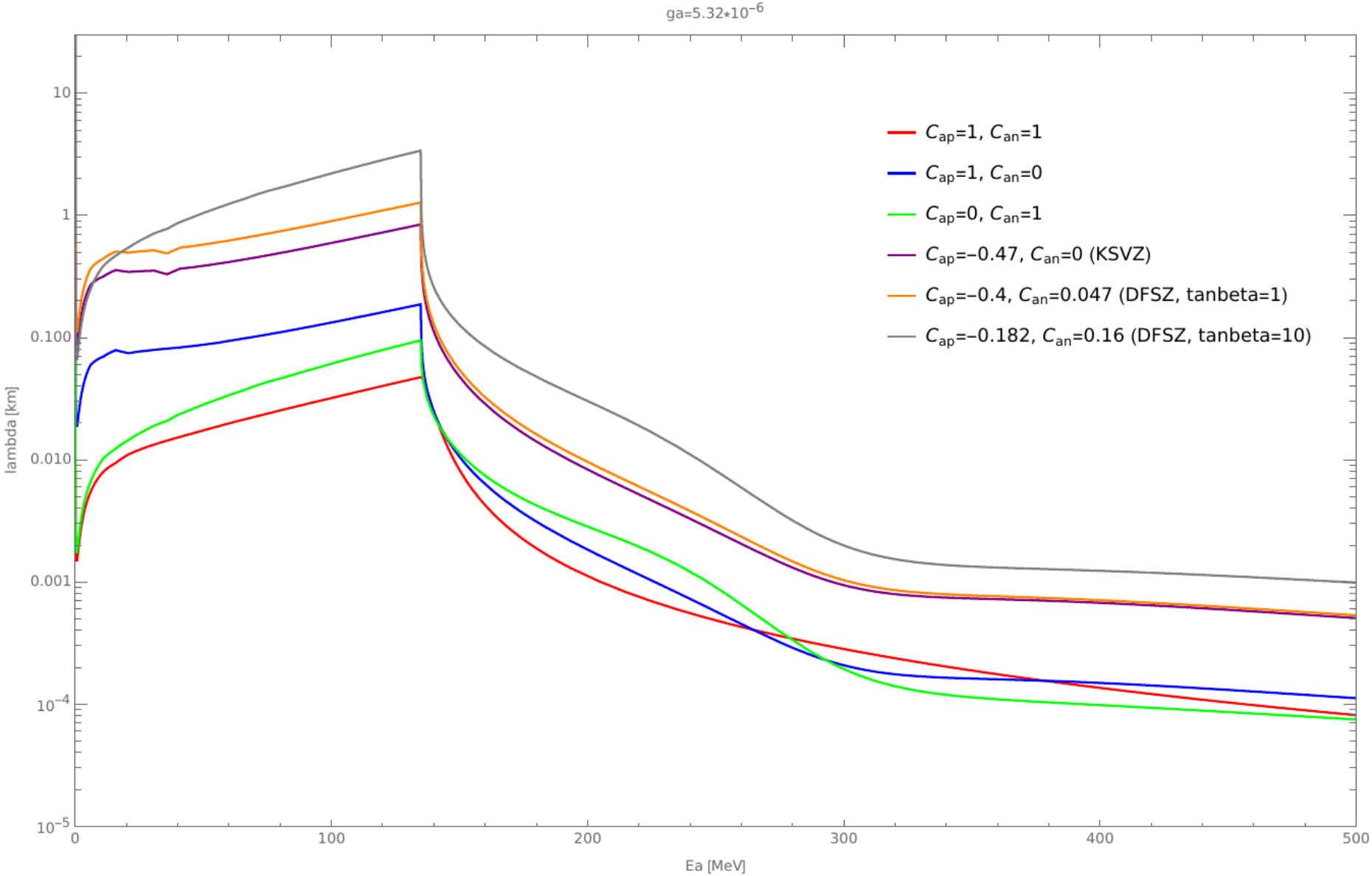

Mean-free path

$R = 15$ km, $g_a = 5\,10^{-6}$, massless ALPs

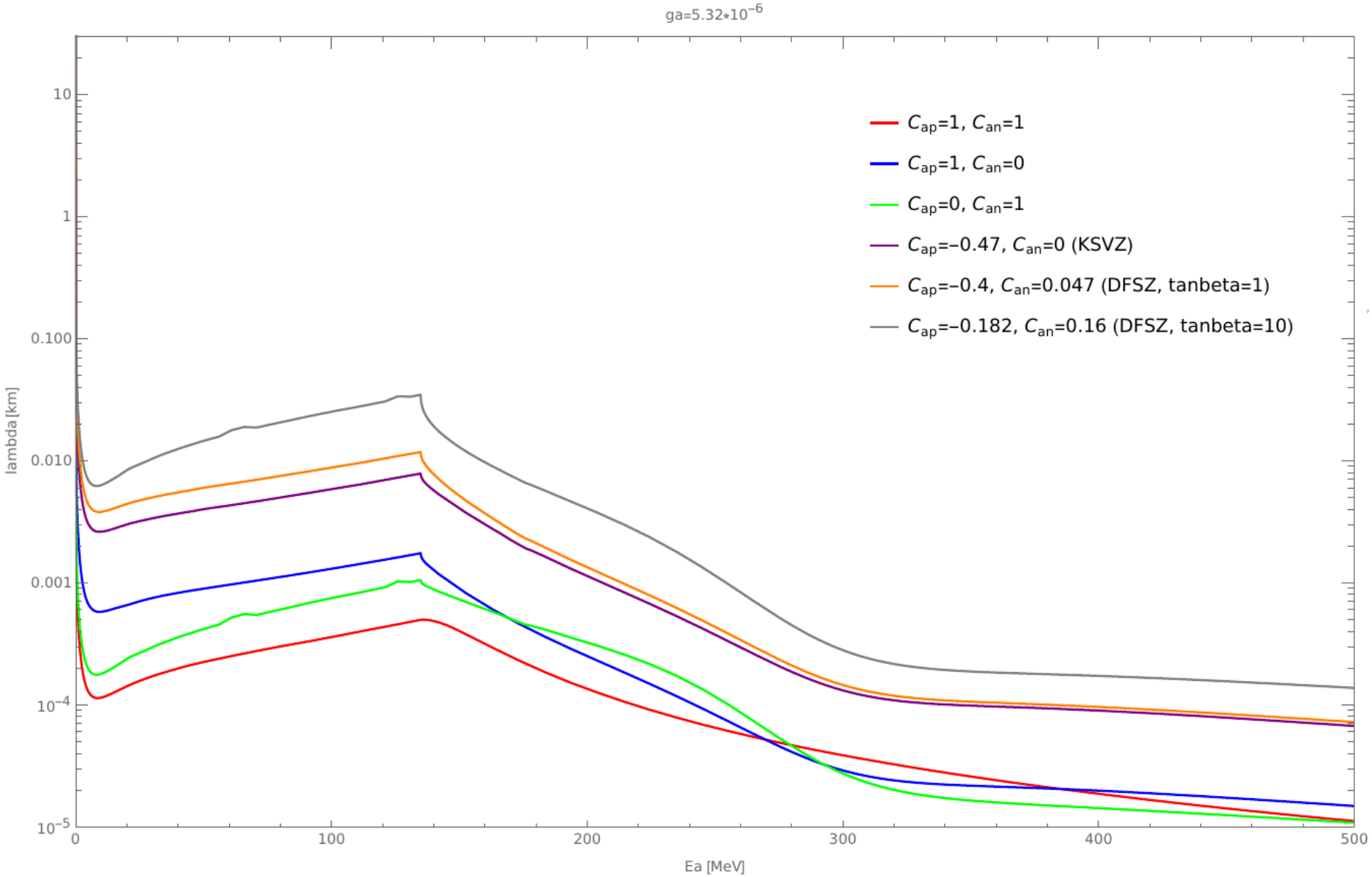

Mean-free path

$R = 10$ km, $g_a = 5\,10^{-6}$, massless ALPs

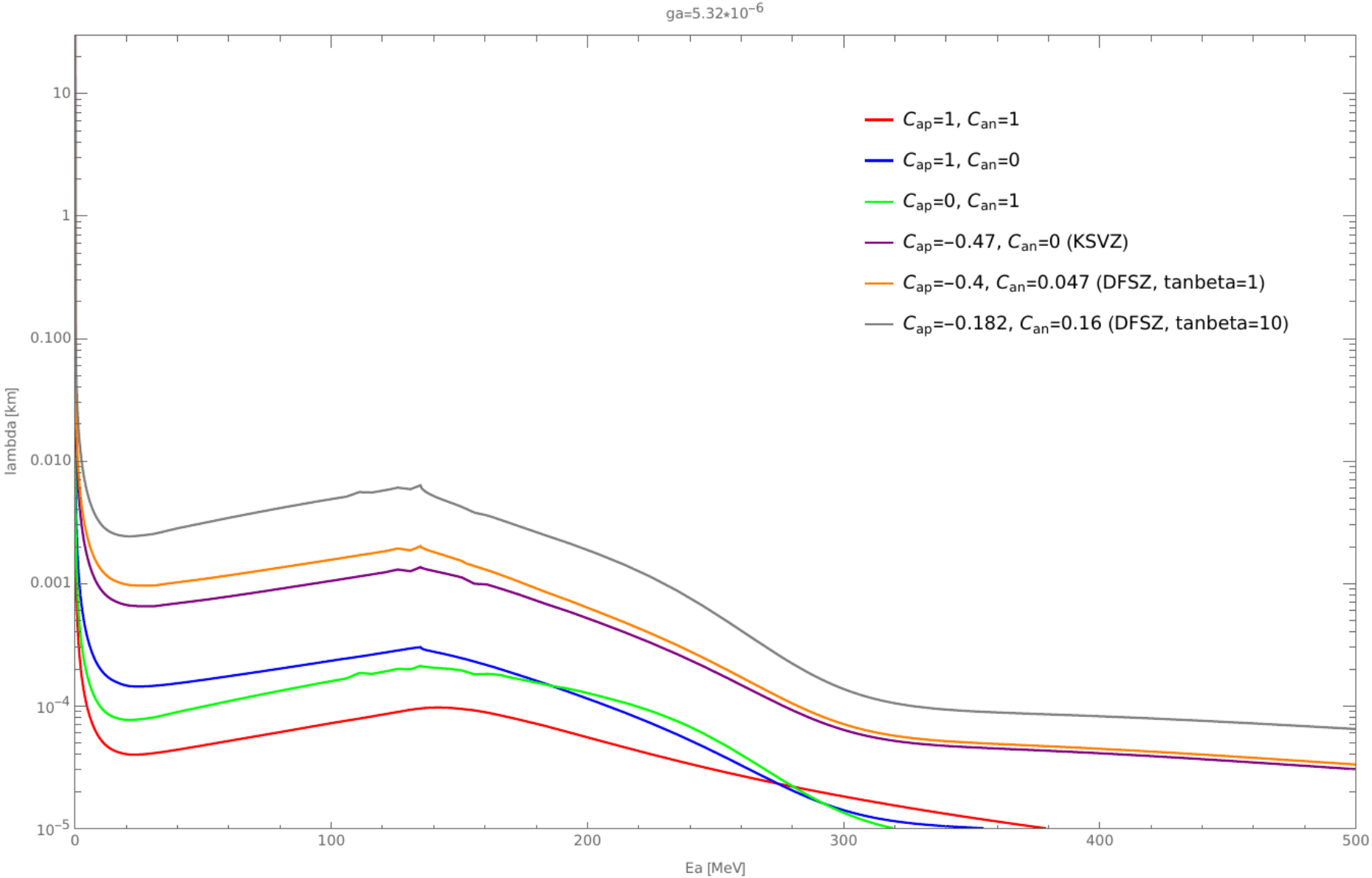

Mean-free path

$R = 5$ km, $g_a = 5\,10^{-6}$, massless ALPs

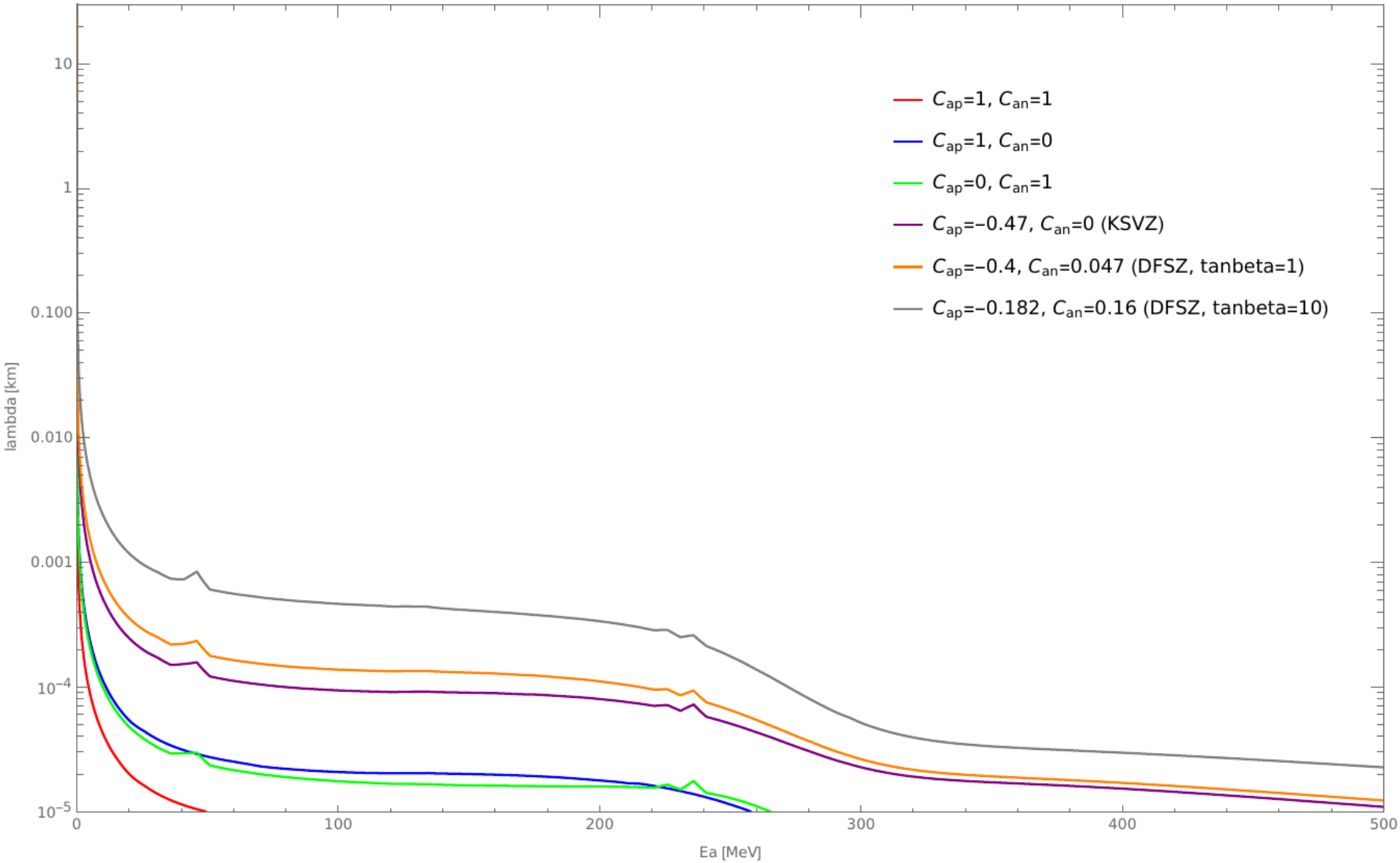

Feynman amplitude for $a\,p \to p\,\gamma$

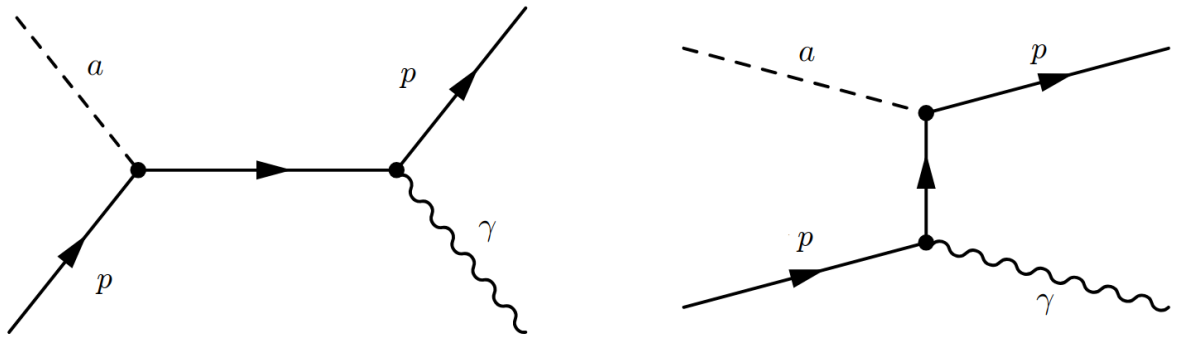

$$a(p_1) + p(p_2) \to p(p_3) + \gamma(p_4)$$

$$\mathcal{M}_s = \bar{u}(p_3)\left[e\gamma^{\mu}\right]\frac{i}{(\not{p}_1 + \not{p}_2) - m_p}\left[\frac{g_a C_{ap}}{2m_p}\gamma^{\nu}\gamma_5\right]u(p_2)\,(p_1)_{\nu}\,\epsilon^*_{\mu}(p_4)$$

$$\mathcal{M}_t = \bar{u}(p_3)\left[\frac{g_a C_{ap}}{2m_p}\gamma^{\rho}\gamma_5\right]\frac{i}{(\not{p}_3 - \not{p}_1) - m_p}\left[e\gamma^{\lambda}\right]u(p_2)\,(p_1)_{\rho}\,\epsilon^*_{\lambda}(p_4)$$

$$|\overline{\mathcal{M}}|^2 = \frac{C_{ap}^2 e^2 g_a^2}{E_\gamma^2 m_p\left(2E_a m_p + m_a^2\right)^2} \times 4m_p^3(E_a - E_\gamma)^2\left(2E_a E_\gamma + m_a^2\right)$$

$$+ \quad 4m_a^2 m_p^2(E_a - E_\gamma)\left(E_\gamma(E_a - E_\gamma) + m_a^2\right) + m_a^4 m_p\left(2E_a E_\gamma + m_a^2\right) + E_\gamma m_a^6$$

Feynman amplitude dipole interaction

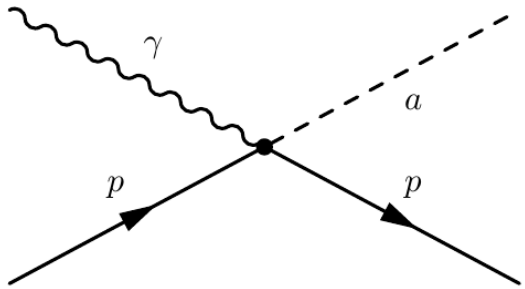

$$a(p_1) + p(p_2) \rightarrow p(p_3) + \gamma(p_4)$$

$$\mathcal{M}_{\text{dipole}} = \bar{u}(p_3)\left[-\frac{i}{2} g_{d,p}\gamma_5\sigma^{\mu\nu}\right]\bar{u}(p_2)\left[(p_4)_\mu \epsilon^*_\nu(p_4) - (p_4)_\nu \epsilon^*_\mu(p_4)\right]$$

$$g_{d,N} = \frac{C_{ap\gamma}\, g_a}{m_N^2},\ C_{ap\gamma} = 0.0033$$

$$|\overline{\mathcal{M}}|^2_{\text{dipole}} = 8C^2_{ap\gamma} g_a^2 \frac{E_\gamma\left(2E_a m_p + m_a^2\right)}{m_p^3}$$

Differential cross section $a\,p \to \gamma\,p$

$$\frac{d\sigma_a}{dE_\gamma} = \int \frac{1}{32\pi} \frac{\left|\overline{\mathcal{M}}\right|^2}{|\vec{p_a}|^2 m_A}\, d\cos\theta\, \delta(\cos\theta - \cos\theta^0)$$

the cosine of the angle between the photon and ALP momenta is fixed by energy conservation

$$\cos\theta_0 = \frac{2E_\gamma(m_p + E_a) - 2m_p E_a - m_a^2}{2E_\gamma\sqrt{E_a^2 - m_a^2}}$$

$|\cos\theta^0| \leq 1 \Rightarrow E_\gamma^{min}(E_a),\, E_\gamma^{max}(E_a)$ or $E_a^{min}(E_\gamma),\, E_a^{max}(E_\gamma)$

$$E_\gamma^{\min} = \frac{m_a^2 + 2E_a m_p}{2(m_p + E_a) + 2\sqrt{E_a^2 - m_a^2}} \qquad E_\gamma^{\max} = \frac{m_a^2 + 2E_a m_p}{2(m_p + E_a) - 2\sqrt{E_a^2 - m_a^2}}$$

For $1\,\text{MeV} < E_a < 100\,\text{MeV}$, $10^{-3}\,\text{MeV} < E_\gamma^{\max} - E_\gamma^{\min} < 18\,\text{MeV}$

ALP-nucleon photo-production cross section: comparison with nucleon electric-dipole portal

For $m_a = 20$ MeV, $E_a = 30$ MeV and $g_a = 5 \cdot 10^{-5}$

$$\sigma \sim 7.50 \times 10^{-41} \text{ cm}^2$$

$$\sigma_{\text{dipole}} \sim 1.11 \times 10^{-43} \text{ cm}^2$$

Spread in the arrival time of ALPs

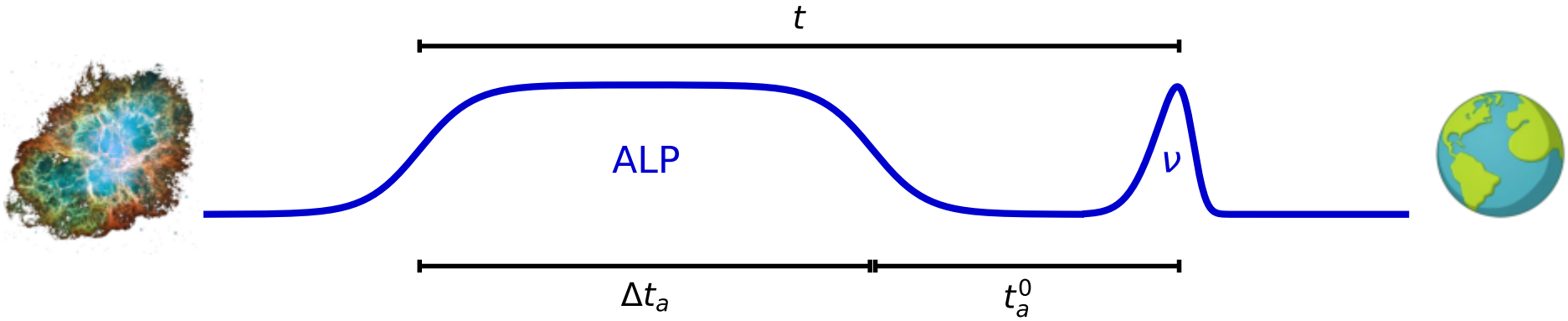

$$t_a = \frac{d}{v_a} = \frac{d}{\sqrt{1-\left(\frac{m_a}{E_a}\right)^2}} \Rightarrow \Delta t_a = t^{\max} - t^{\min} = d\left(\frac{1}{\sqrt{1-\left(\frac{m_a}{E_a^{\min}}\right)^2}} - \frac{1}{\sqrt{1-\left(\frac{m_a}{E_a^{\max}}\right)^2}}\right) = d\frac{\sqrt{1-\left(\frac{m_a}{E_a^{\max}}\right)^2} - \sqrt{1-\left(\frac{m_a}{E_a^{\min}}\right)^2}}{\sqrt{1-\left(\frac{m_a}{E_a^{\min}}\right)^2}\sqrt{1-\left(\frac{m_a}{E_a^{\max}}\right)^2}}$$

$$\Delta t_a = \frac{d\Delta v}{\sqrt{1-\left(\frac{m_a}{E_a^{\min}}\right)^2}\sqrt{1-\left(\frac{m_a}{E_a^{\max}}\right)^2}} \simeq \frac{d\Delta v}{\bar{v}^2}$$

Background Super-Kamiokande

Super-Kamiokande Collaboration, PRD 104 (2021) 122002

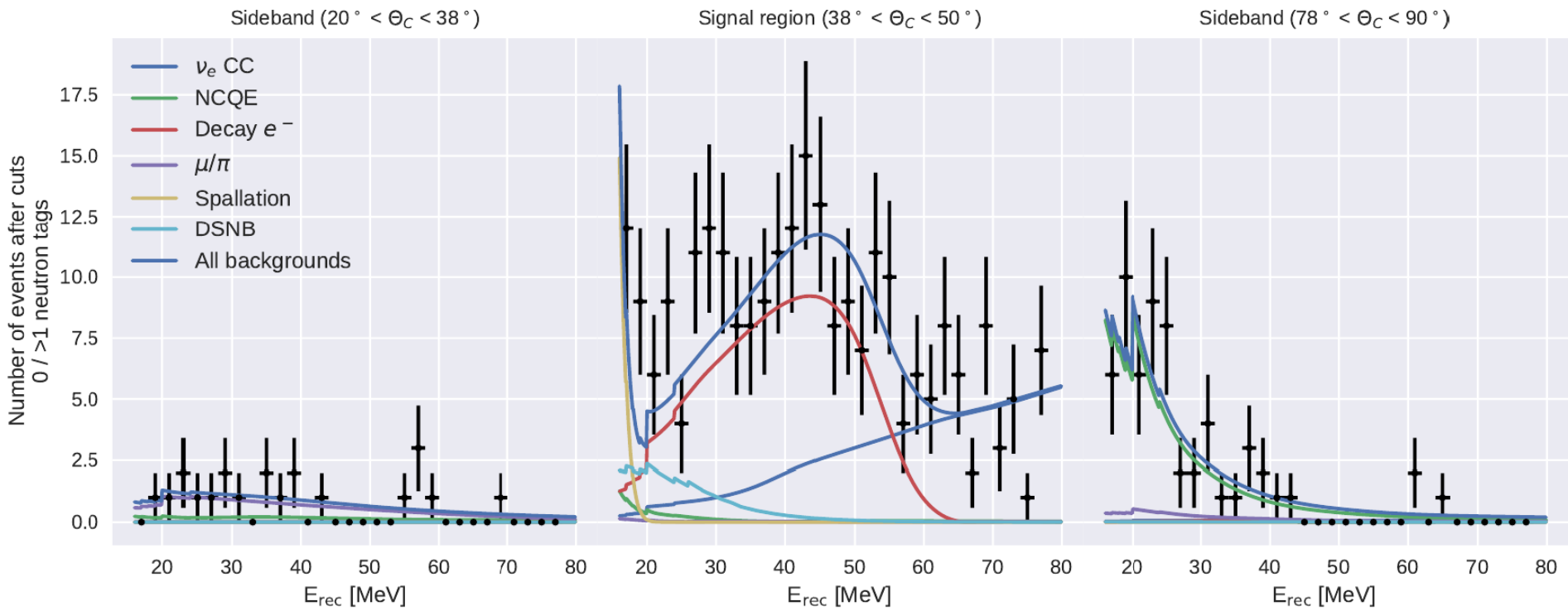

Background Hyper-Kamiokande

Hyper-Kamiokande Collaboration, e-Print: 1805.04163

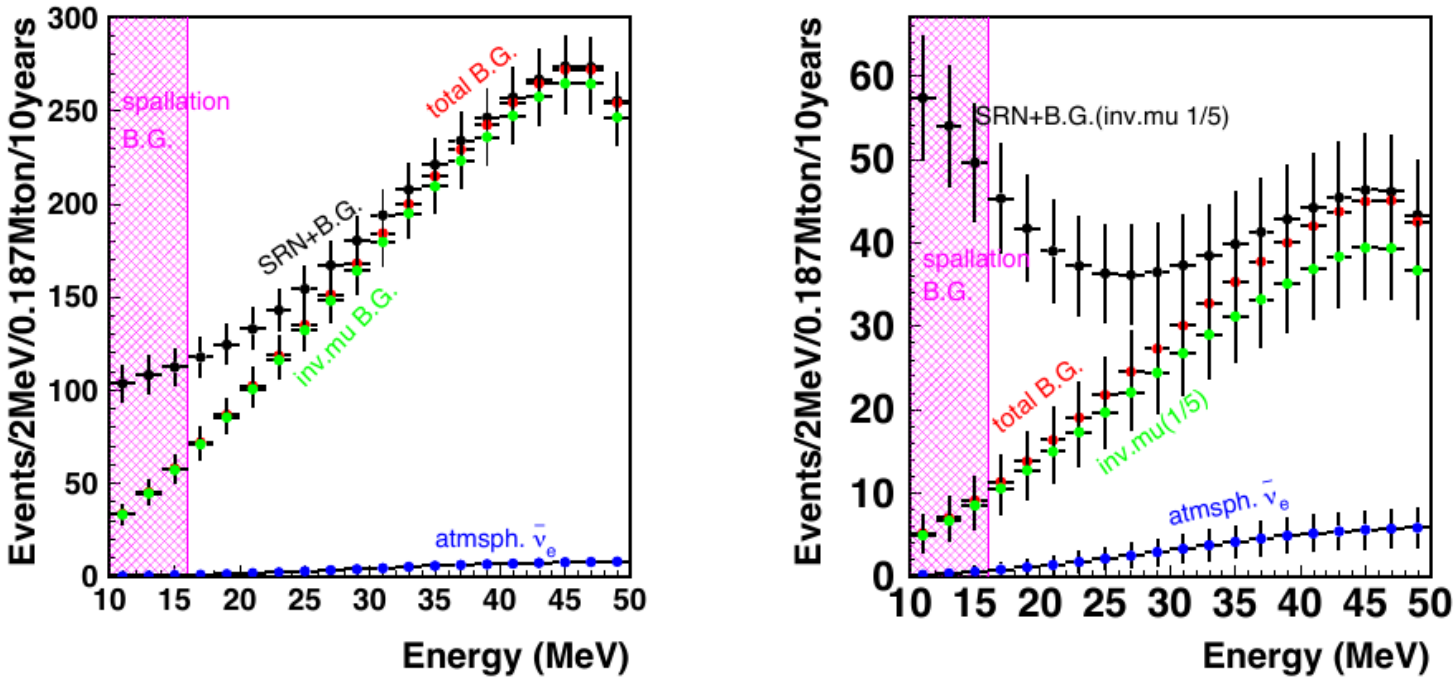

FIG. 188. Expected spectrum of SRN signals at Hyper-K with 10 years of livetime without tagging neutrons. Left figure shows the case without tagging neutrons, assuming a signal selection efficiency of 90%. Neutron tagging were applied for right figure, with the tagging efficiency of 67% and the pre-gamma cut for invisible muon background reduction. The black dots show the sum of the signal and the total background, while the red shows the total background. Green and blue show background contributions from the invisible muon and ν_e components of atmospheric neutrinos. The SRN flux prediction in [296] is applied.

Constraints from SK and projections for HK

Profiled log-likelihood-ratio test

$$q(\theta) = -2 \ln \left(\frac{\mathcal{L}(\theta)}{\mathcal{L}(\hat{\theta})} \right)$$

Binned statistical treatment assuming that the number of events in each bin follows a Poisson distribution,

$$q(\theta) = 2 \left[\sum_{i=1}^{n_{bins}} N^i_{th}(\theta) - N^i_{\rm obs} + N^i_{\rm obs} \ln \left(\frac{N^i_{\rm obs}}{N^i_{th}(\theta)} \right) \right]$$

follows a χ^2 distribution.

For the projected exclusion limits for HK:

$$Z(\theta) = \left[2 \sum_{i=1}^{n_{bins}} S^i_{th}(\theta) + B^i_{th} \ln \left(\frac{B^i_{th}}{S^i_{th}(\theta) + B^i_{th}} \right) \right]^{1/2}$$

95% C.L. at Z = 1.96

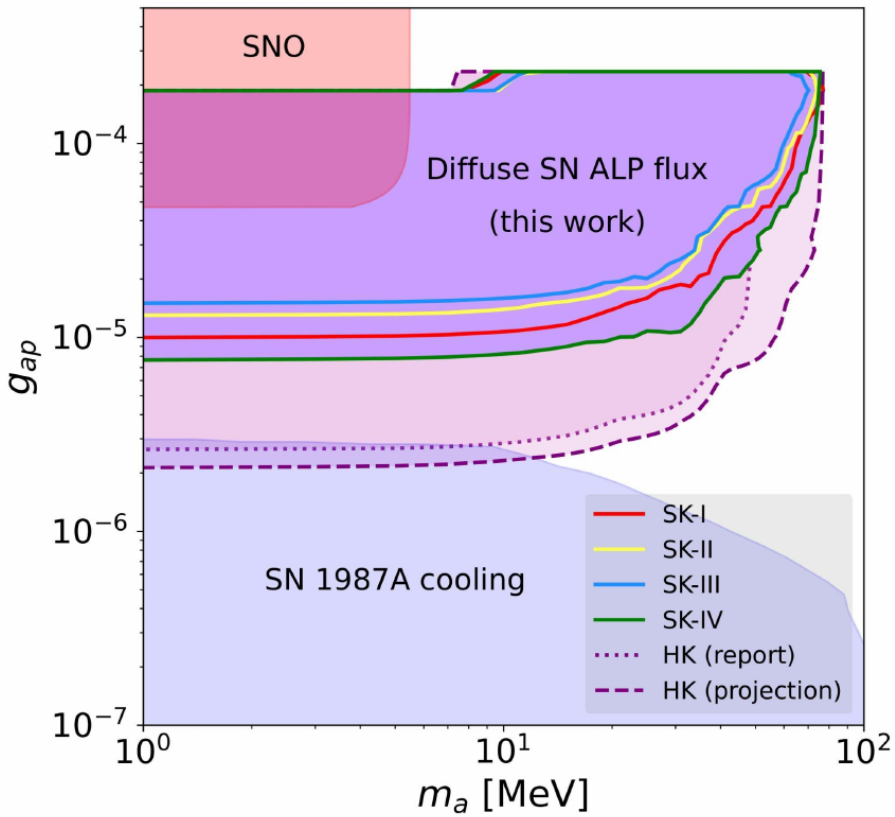

Constraints from SK and projections for HK

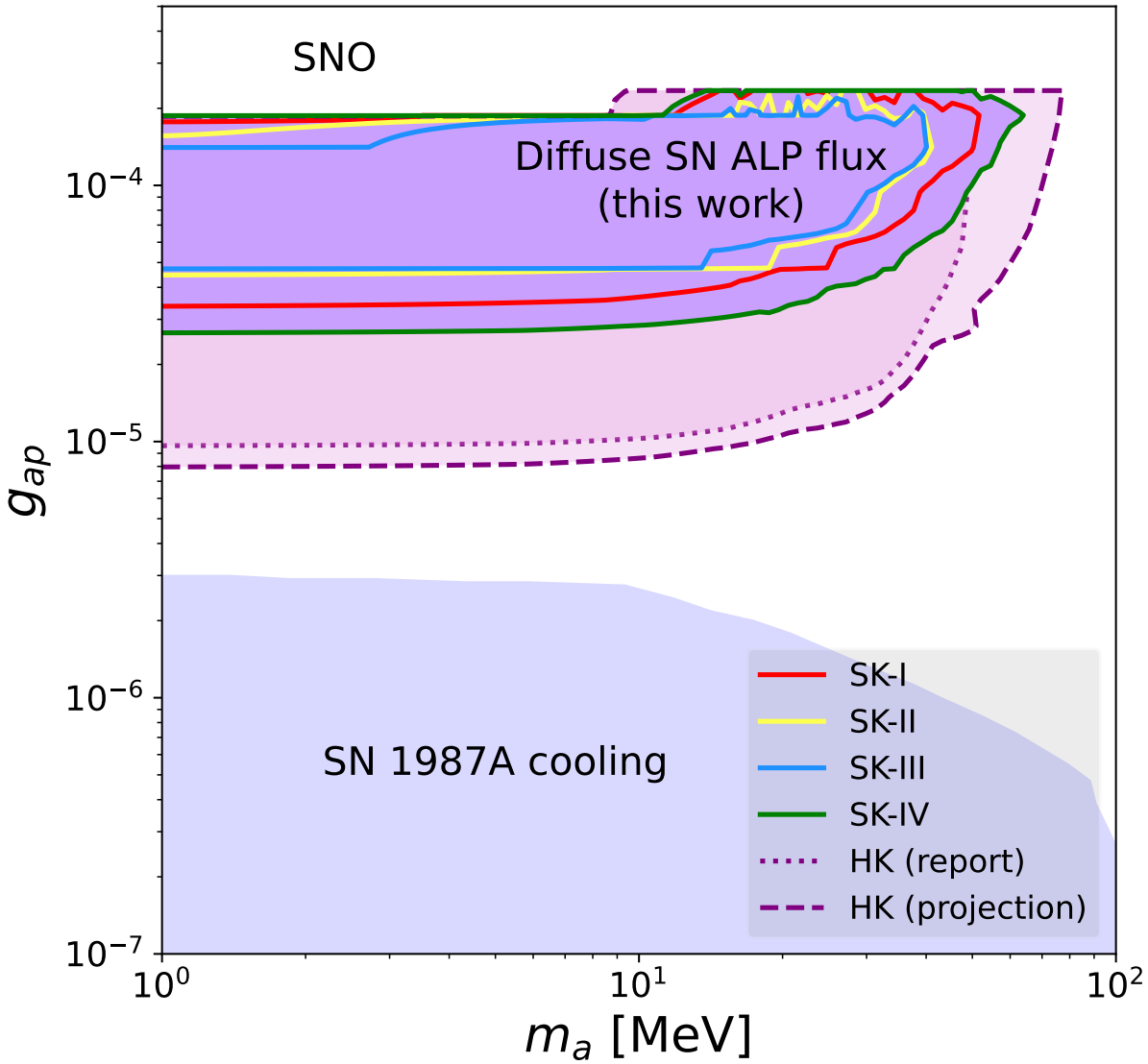

Simulation: Diffuse ALP flux from galactic SNe

Galactic SN rate and distribution:

$$\frac{dn_{SN}}{dt} = A\, \mathrm{e}^{-\frac{r}{R_d}}\, \mathrm{e}^{-\frac{|z|}{H}}$$

For ccSNe:

$R_d \simeq 2.6$ kpc H=0.3kpc

SN rate: 1.63 per century

$A = 1.65 \times 10^{-3}$ kpc^{-3} yr^{-1}

Simulation

```
SN time window: 6.34e+05 [yr]
Average number of expected SNe: 13237.29

Iteration | SN count
        1 |    13441
        2 |    13268
        3 |    13136
        4 |    13222
        5 |    13071
        6 |    13104
        7 |    13281
        8 |    13045
        9 |    13271
       10 |    13388
       11 |    13127
       12 |    13288
       13 |    13245
       14 |    13033
```

SN position w.r.t GC

$t_{today} - t_{SN}$

	r [kpc]	θ	z [kpc]	t [s]
0	0.122868	1.283047	0.051144	1.037383e+10
1	1.772018	1.381232	0.305451	1.079115e+10
2	1.182192	3.705303	0.028299	1.440616e+10
3	5.563034	2.271368	-0.097046	1.531587e+10
4	1.073842	2.382373	0.026703	1.821946e+10
5	2.203187	5.402907	-0.146469	1.824385e+10
6	0.735043	2.982268	0.140886	2.085627e+10
7	1.950696	3.040194	0.202884	2.292907e+10
8	2.748263	4.606353	0.118484	2.599070e+10
9	2.712416	1.668001	-0.165745	2.856984e+10

Simulation: Diffuse ALP flux from galactic SNe

The position of the last 200 SN (simulated)

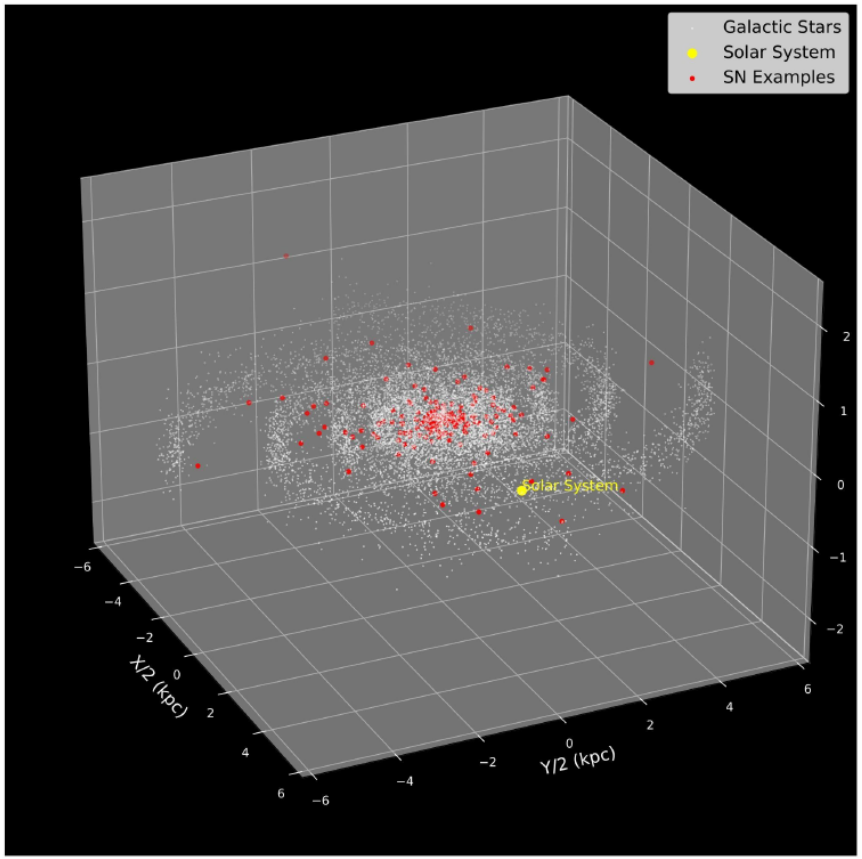

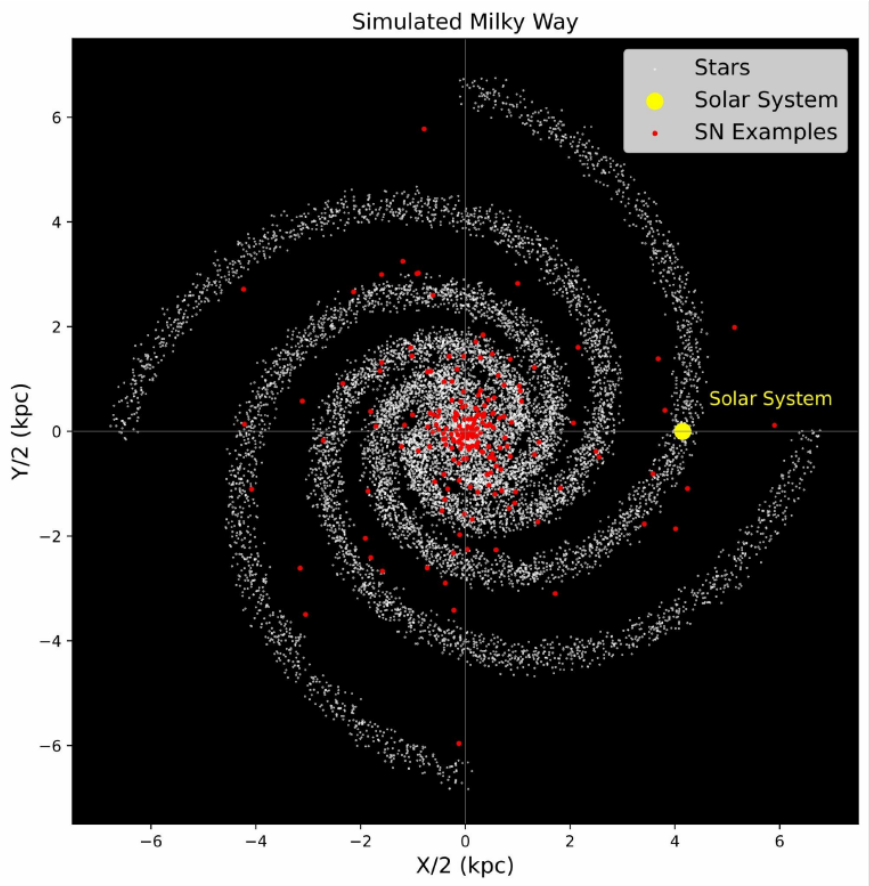

Simulation: Diffuse ALP flux from galactic SNe

$$flux\,factor = \int_{-\infty}^{\infty}\int_{0}^{2\pi}\int_{0}^{\infty} \frac{dn_{SN}}{dt}\,\frac{r}{4\pi\,(\vec{r}-\vec{R}_E)^2}\,dr\,d\theta\,dz$$

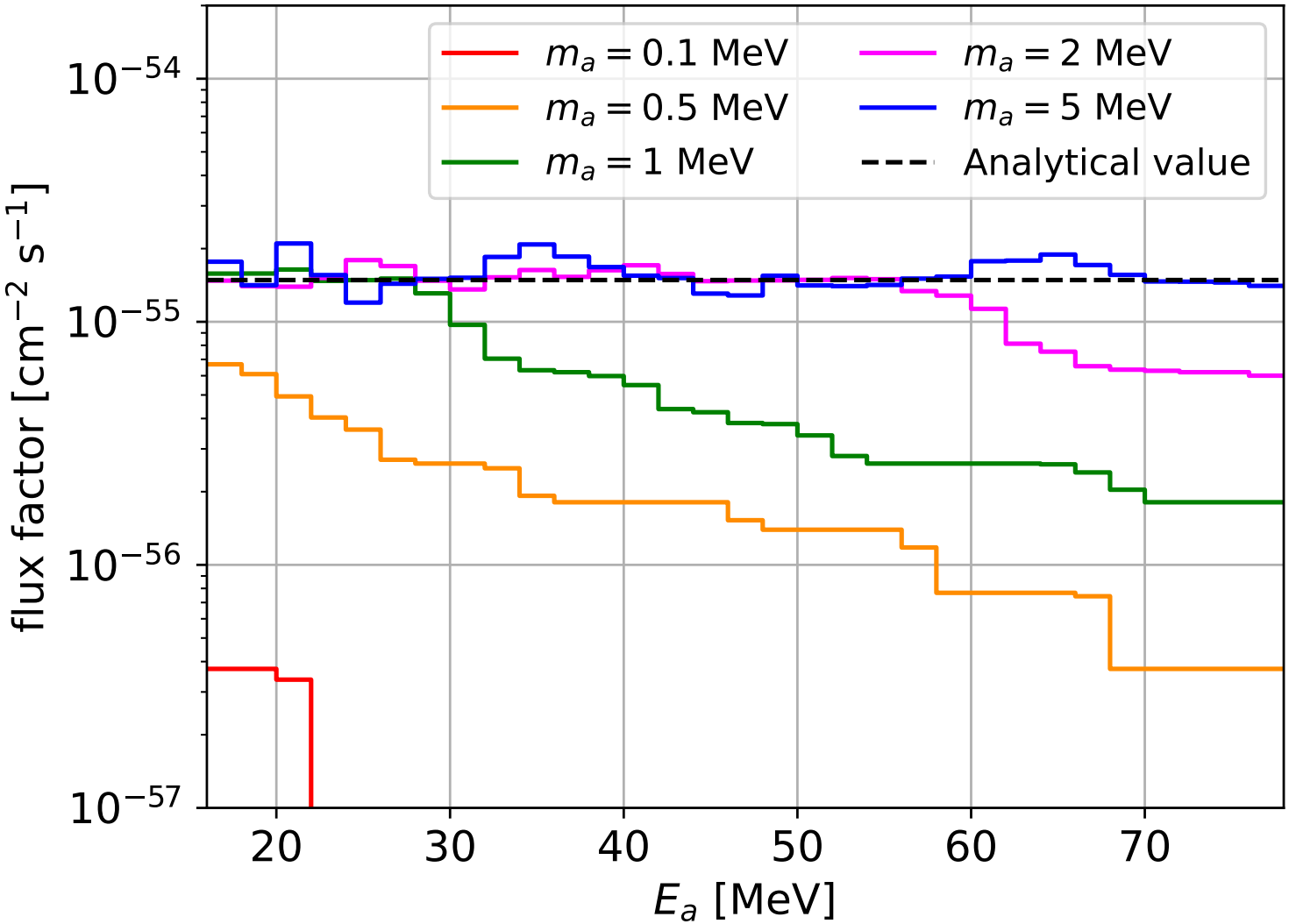

Sensitivity future galactic SN

*D. Alonso-González, D. Cerdeño, **M. Cermeño**, A. D. Perez, PRD 111 (2025) 8, 083029*

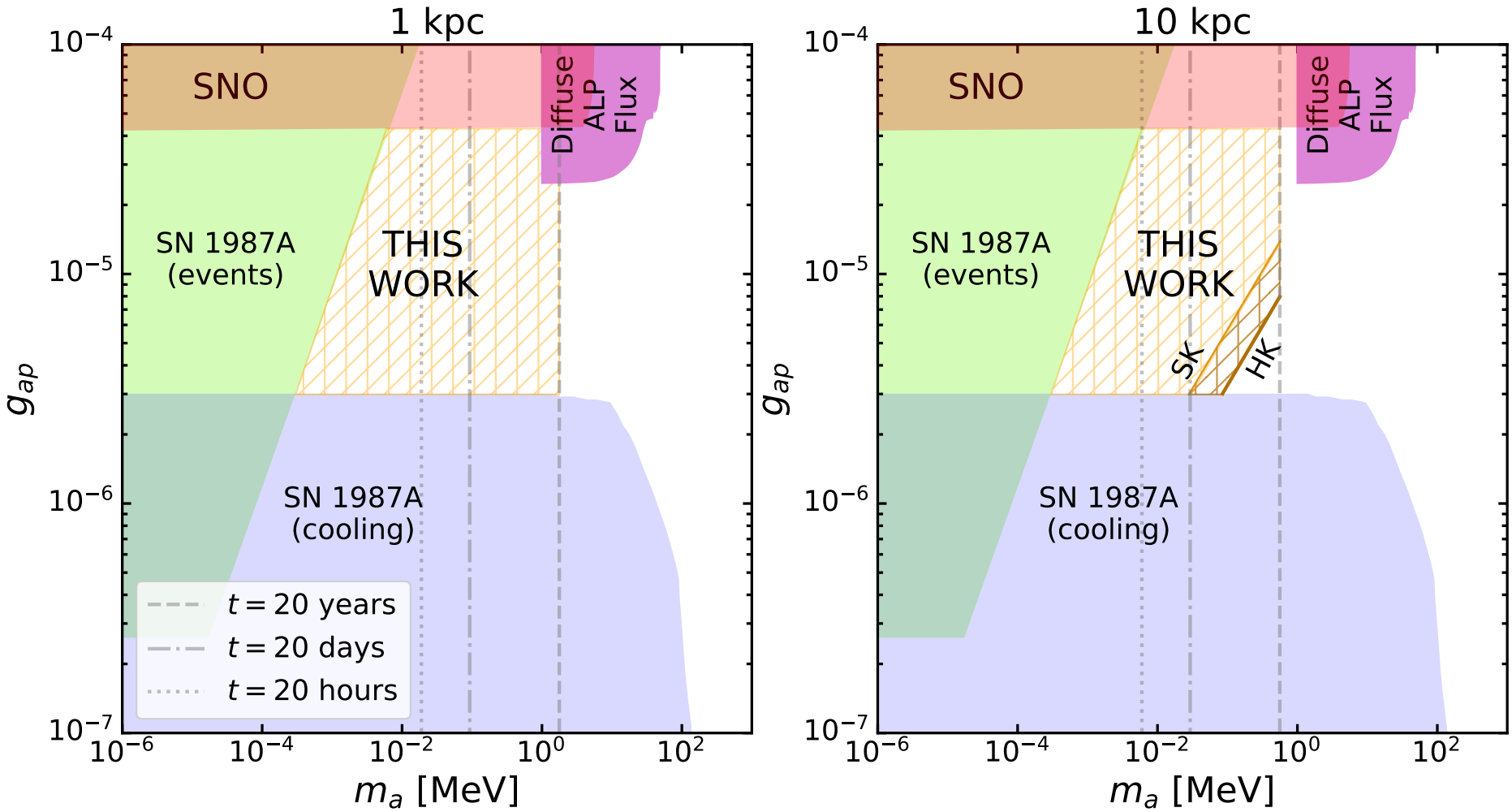

Sensitivity future galactic SN

*D. Alonso-González, D. Cerdeño, **M. Cermeño**, A. D. Perez, PRD 111 (2025) 8, 083029*

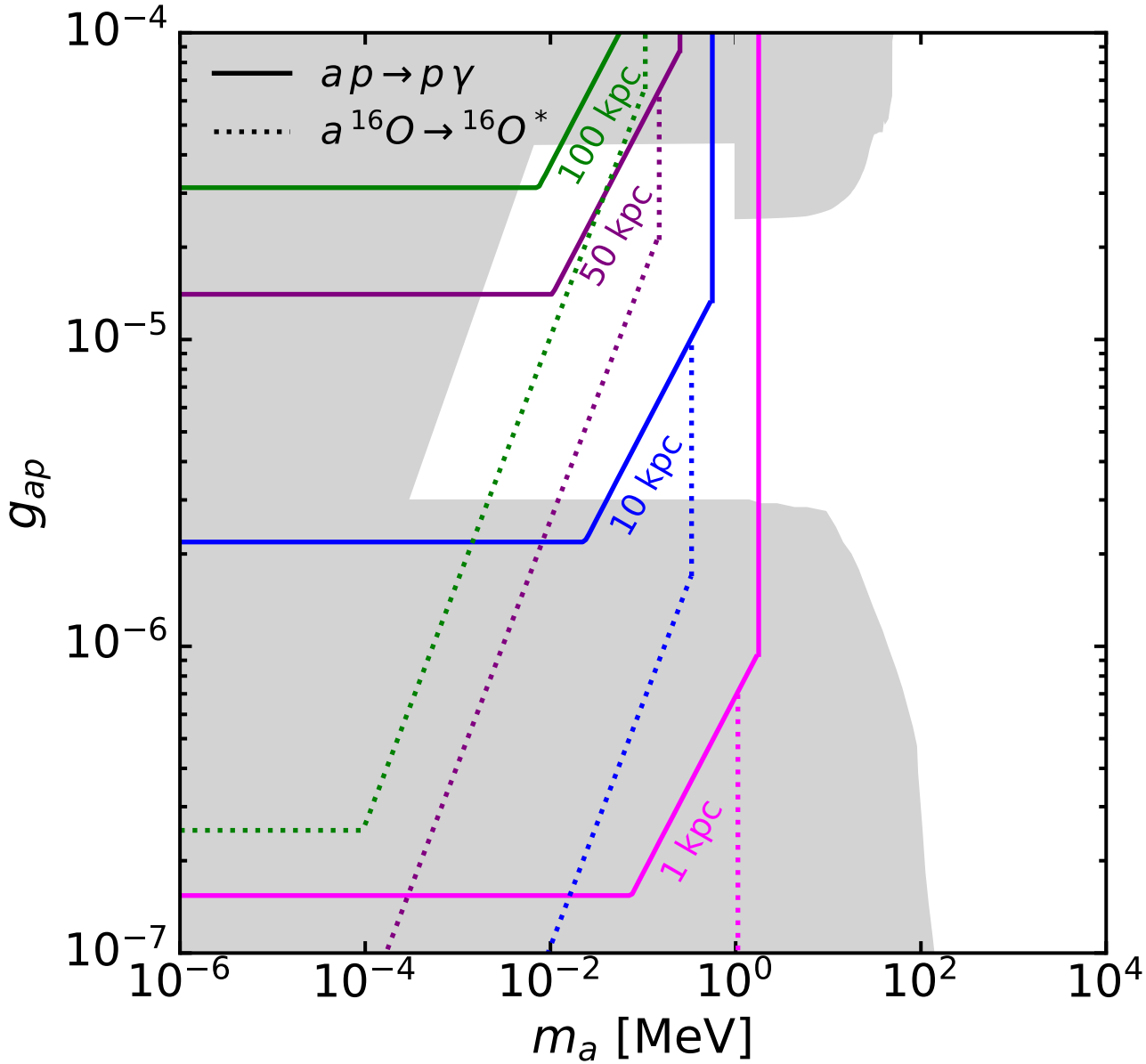

Proto-NS birth

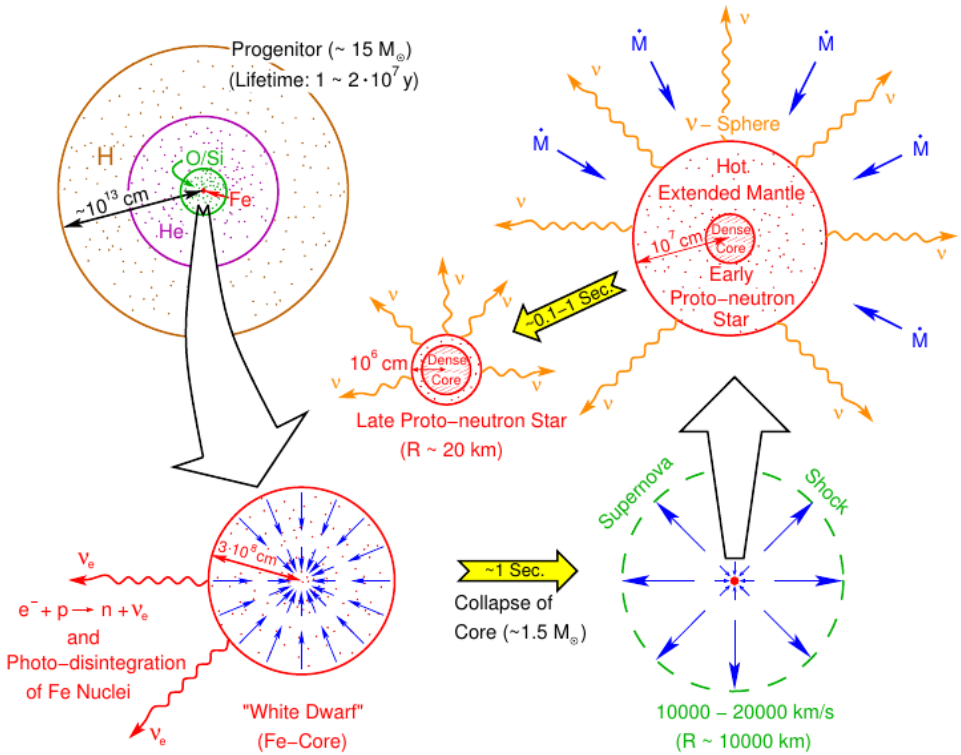

Fig. 2 Evolution of a massive star from the onset of iron-core collapse to a neutron star. The progenitor has developed a typical onion-shell structure with layers of increasingly heavier elements surrounding the iron core at the center (upper left corner). Like a white dwarf star, this iron core (enlarged on the lower left side) is stabilized mostly by the fermion pressure of nearly degenerate electrons. It becomes gravitationally unstable when the rising temperatures begin to allow for partial photo-disintegration of iron-group nuclei to α-particles and nucleons. The contraction accelerates to a dynamical collapse by electron captures on bound and free protons, releasing electron neutrinos (ν_e), which initially escape freely. Only fractions of a second later, the catastrophic infall is stopped because nuclear-matter density is reached and a proto-neutron star begins to form. This gives rise to a strong shock wave which travels outward and disrupts the star in a supernova explosion (lower right). The nascent neutron star is initially very extended (enlarged in the upper right corner), and contracts to a more compact object while accreting more matter (visualized by the mass-accretion rate $\dot{M}$) within the first second of its evolution. This phase as well as the subsequent cooling and neutronization of the compact remnant are driven by the emission of neutrinos and antineutrinos of all flavors (indicated by the symbol ν), which diffuse out from the dense and hot super-nuclear core over tens of seconds. (Figure adapted from Burrows 1990b)

Neutrino luminosity

Fischer et al., PRD 85 (2012) 083003

$$M_{\rm proj} = 18\,M_\odot$$

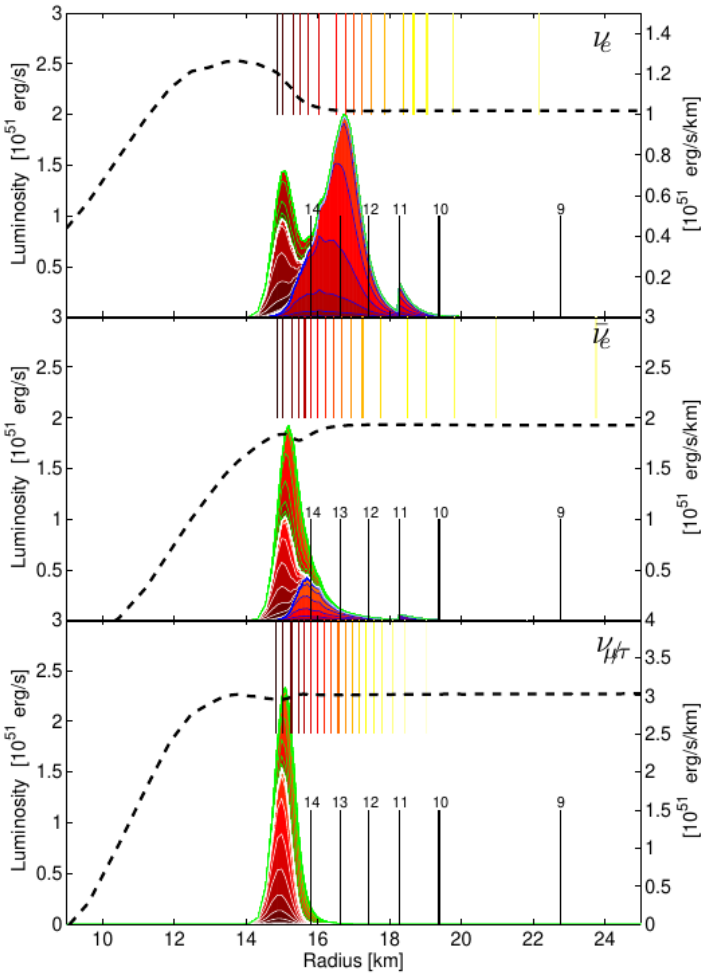

(a) 5 seconds post bounce

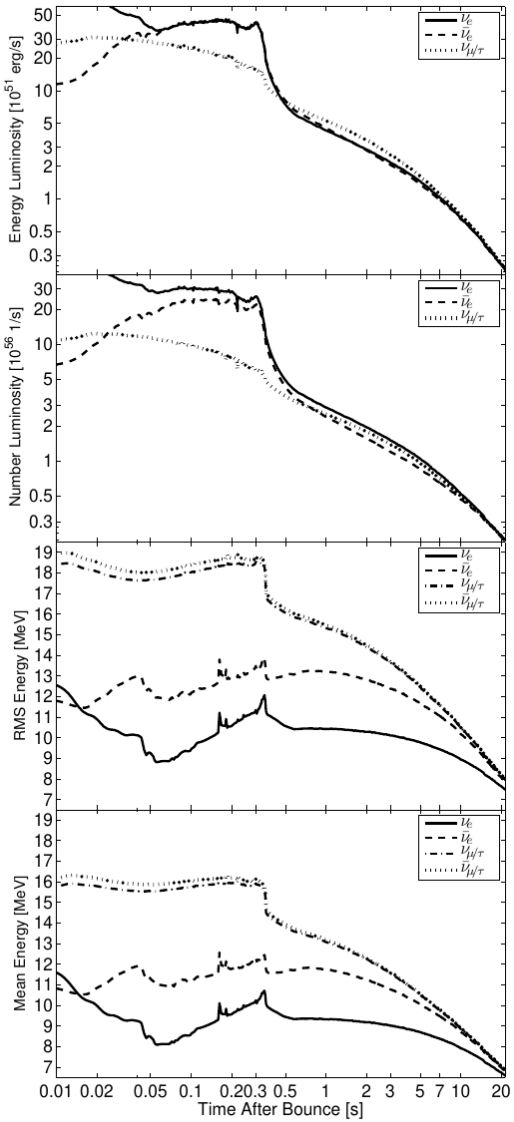

SN neutrinos

ν's are crucial in proto-NS evolution $\Rightarrow$ good sites to test new ν interactions

During the final phases of core collapse SN ν's are copiusly produced in the proto-NS interior ($n_\nu \sim 10^{36}\,\mathrm{cm}^{-3}$) and trapped due to their scattering with Ns
After a second, they are emitted as the star cools down (Kelvin-Helmholtz cooling)

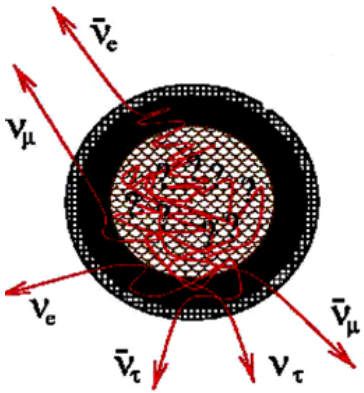

- Emitted ν's observed during $t_{\mathrm{signal}} \sim 10$ s from the SN 1987A
- t_{signal} proportional to the ν diffusion time in the stellar material $t_{\mathrm{signal}} \sim 10\, t_{\mathrm{diff}}$
- The observed emision time is compatible with the one predicted by the SM

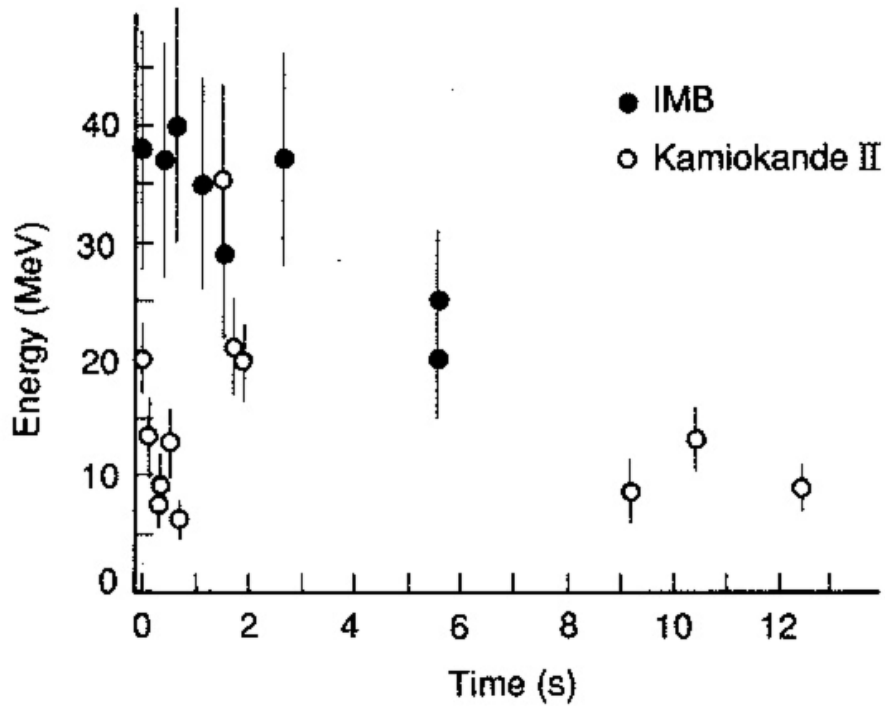

Relevant interactions inside SN

Janka arXiv: 1702.08713. In 'Handbook of Supernovae,' Springer

Table 1 Most important neutrino processes in supernova and proto-neutron star matter.

Process	Reaction[a]
Beta-processes (direct URCA processes)	
electron and ν_e absorption by nuclei	$e^- + (A,Z) \longleftrightarrow (A,Z-1) + \nu_e$
electron and ν_e captures by nucleons	$e^- + p \longleftrightarrow n + \nu_e$
positron and $\bar{\nu}_e$ captures by nucleons	$e^+ + n \longleftrightarrow p + \bar{\nu}_e$
"Thermal" pair production and annihilation processes	
Nucleon-nucleon bremsstrahlung	$N + N \longleftrightarrow N + N + \nu + \bar{\nu}$
Electron-position pair process	$e^- + e^+ \longleftrightarrow \nu + \bar{\nu}$
Plasmon pair-neutrino process	$\widetilde{\gamma} \longleftrightarrow \nu + \bar{\nu}$
Reactions between neutrinos	
Neutrino-pair annihilation	$\nu_e + \bar{\nu}_e \longleftrightarrow \nu_x + \bar{\nu}_x$
Neutrino scattering	$\nu_x + \{\nu_e, \bar{\nu}_e\} \longleftrightarrow \nu_x + \{\nu_e, \bar{\nu}_e\}$
Scattering processes with medium particles	
Neutrino scattering with nuclei	$\nu + (A,Z) \longleftrightarrow \nu + (A,Z)$
Neutrino scattering with nucleons	$\nu + N \longleftrightarrow \nu + N$
Neutrino scattering with electrons and positrons	$\nu + e^{\pm} \longleftrightarrow \nu + e^{\pm}$

[a] N means nucleons, i.e., either n or p, $\nu \in \{\nu_e, \bar{\nu}_e, \nu_\mu, \bar{\nu}_\mu, \nu_\tau, \bar{\nu}_\tau\}$, $\nu_x \in \{\nu_\mu, \bar{\nu}_\mu, \nu_\tau, \bar{\nu}_\tau\}$

Relevant interactions inside SN

Janka arXiv: 1702.08713. In 'Handbook of Supernovae,' Springer

CC β-processes

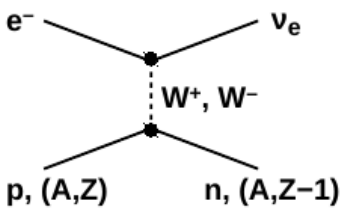

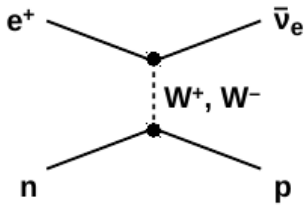

CC scattering process

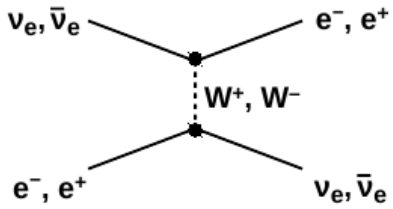

NC scattering processes ($\nu = \nu_e, \bar{\nu}_e, \nu_\mu, \bar{\nu}_\mu, \nu_\tau, \bar{\nu}_\tau$)

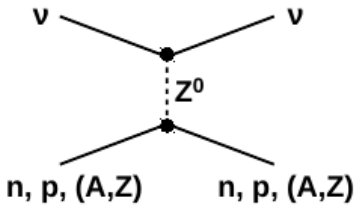

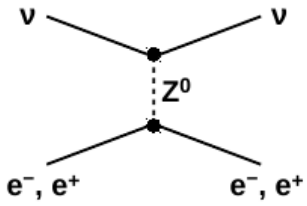

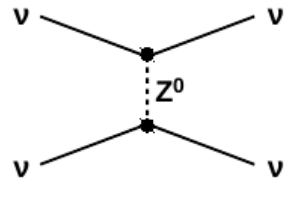

Neutrino-pair ("thermal") processes

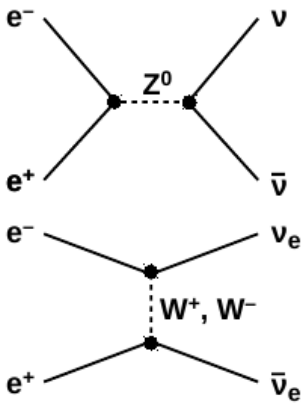

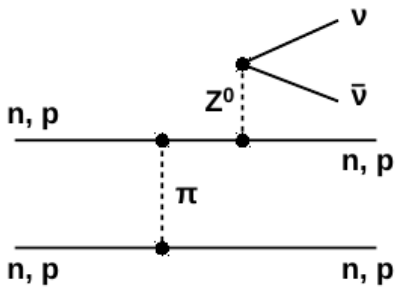

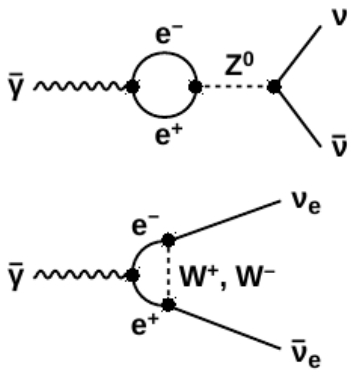

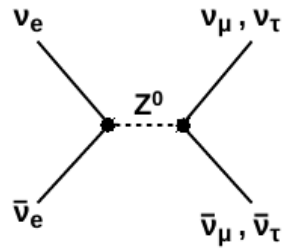

Neutrino decoupling SM

Janka arXiv: 1702.08713. In 'Handbook of Supernovae,' Springer

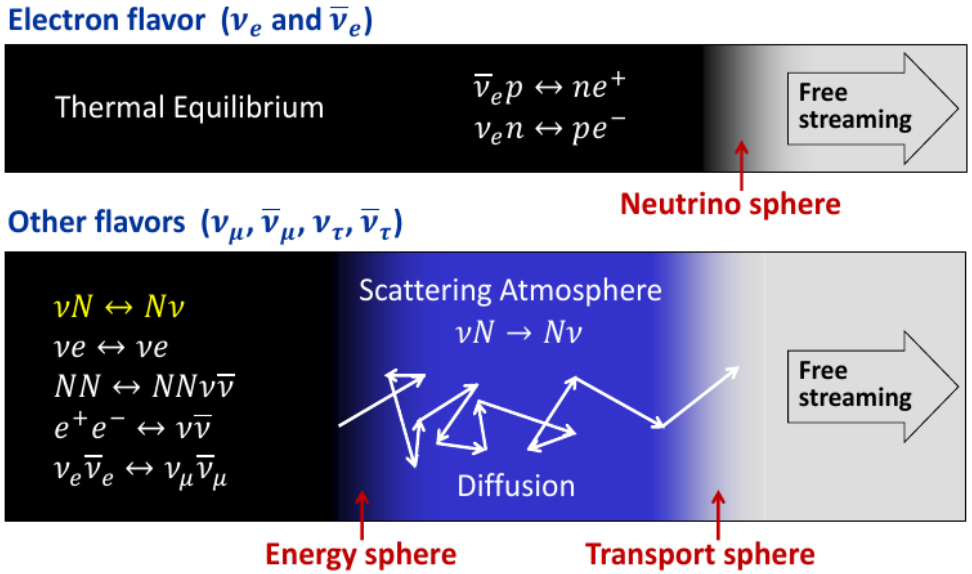

Fig. 4 Sketch of the transport properties of electron-flavor neutrinos and antineutrinos (*upper part*) compared to heavy-lepton neutrinos (*lower part*). In the supernova core ν_e and $\bar{\nu}_e$ interact with the stellar medium by charged-current absorption and emission reactions, which provide a major contribution to their opacities and lead to a strong energetic coupling up to the location of their neutrinospheres, outside of which both chemical equilibrium between neutrinos and stellar matter (indicated by the black region) and diffusion cannot be maintained. In contrast, heavy-lepton neutrinos are energetically less tightly coupled to the stellar plasma, mainly by pair creation reactions like nucleon bremsstrahlung, electron-position annihilation and $\nu_e\bar{\nu}_e$ annihilation. The total opacity, however, is determined mostly by neutrino-nucleon scatterings, whose small energy exchange per scattering does not allow for an efficient energetic coupling. Therefore heavy-lepton neutrinos fall out of thermal equilibrium at an energy sphere that is considerably deeper inside the nascent neutron star than the transport sphere, where the transition from diffusion to free streaming sets in. The blue band indicates the scattering atmosphere where the heavy-lepton neutrinos still collide frequently with neutron and protons and lose some of their energy, but cannot reach equilibrium with the background medium any longer. (Figure adapted from Raffelt 2012 courtesy of Georg Raffelt)

SN phases

Janka arXiv: 1702.08713. In 'Handbook of Supernovae,' Springer

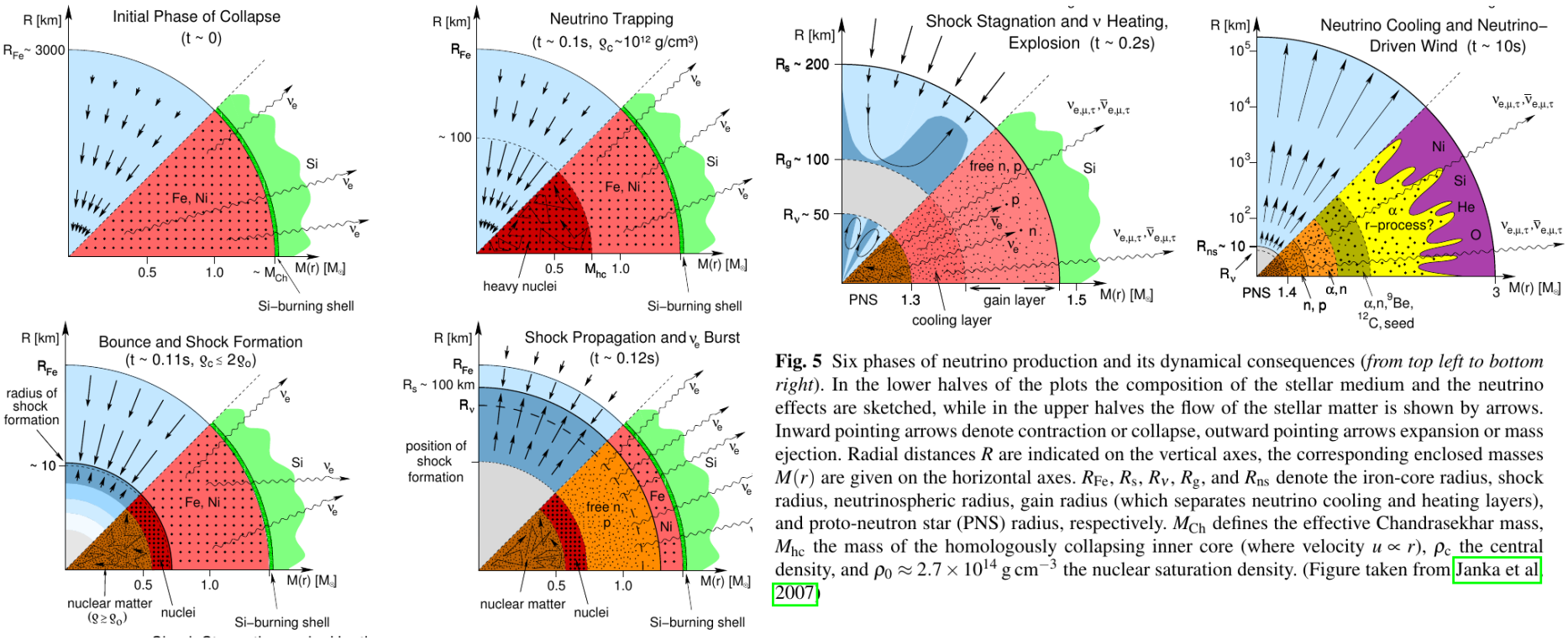

Fig. 5 Six phases of neutrino production and its dynamical consequences (*from top left to bottom right*). In the lower halves of the plots the composition of the stellar medium and the neutrino effects are sketched, while in the upper halves the flow of the stellar matter is shown by arrows. Inward pointing arrows denote contraction or collapse, outward pointing arrows expansion or mass ejection. Radial distances R are indicated on the vertical axes, the corresponding enclosed masses $M(r)$ are given on the horizontal axes. $R_{\rm Fe}$, $R_{\rm s}$, $R_{\rm v}$, $R_{\rm g}$, and $R_{\rm ns}$ denote the iron-core radius, shock radius, neutrinospheric radius, gain radius (which separates neutrino cooling and heating layers), and proto-neutron star (PNS) radius, respectively. $M_{\rm Ch}$ defines the effective Chandrasekhar mass, $M_{\rm hc}$ the mass of the homologously collapsing inner core (where velocity $u \propto r$), $\rho_{\rm c}$ the central density, and $\rho_0 \approx 2.7 \times 10^{14}\,{\rm g\,cm^{-3}}$ the nuclear saturation density. (Figure taken from Janka et al 2007)

Description of the proto-neutron star interior

- The temperature, T, baryonic density, n_B, and electron fraction, Y_e, profiles at 1 s after the bounce from SN simulations *Fischer et al., PRD 85 (2012) 083003*
- The neutron, proton and electron neutrino chemical potentials, μ_n^*, μ_p^* and $\mu_{\nu_e}^*$, and the nucleon effective mass $m_N^\star$ obtained solving the equations of motion and setting the equilibrium conditions Cerdeño, **Cermeño**, Pérez-García and Reid, PRD 104 (2021) 063013

	R (km)	T (MeV)	n_B(fm^{-3})	Y_e	μ_n^* (MeV)	μ_p^* (MeV)	$\mu_{\nu_e}^*$ (MeV)	$m_N^\star$ (MeV)
$k=1$	5.0	15	0.5	0.3	496.6	405.4	114.6	249.6
$k=2$	7.5	20	0.3	0.28	530.0	458.3	102.7	384.9
$k=3$	10.0	28	0.15	0.25	656.5	601.9	79.9	599.4
$k=4$	15.0	33	0.06	0.2	779.8	723.0	29.0	786.0
$k=5$	17.5	18	0.03	0.1	858.7	813.1	14.4	857.0
$k=6$	20.0	7	0.008	0.05	917.2	893.9	12.5	915.9

The energy distribution of nucleons and leptons inside the star described by the Fermi-Dirac distribution $f(E) = \frac{1}{1-e^{(E-\mu)/T}}$, where E is the energy of the particle

Neutrino energy distribution inside the proto-NS

	R (km)	T (MeV)	n_B(fm^{-3})	Y_e	μ_n^* (MeV)	μ_p^* (MeV)	$\mu_{\nu_e}^*$ (MeV)	$m_N^\star$ (MeV)
$k=1$	5.0	15	0.5	0.3	496.6	405.4	114.6	249.6
$k=2$	7.5	20	0.3	0.28	530.0	458.3	102.7	384.9
$k=3$	10.0	28	0.15	0.25	656.5	601.9	79.9	599.4
$k=4$	15.0	33	0.06	0.2	779.8	723.0	29.0	786.0
$k=5$	17.5	18	0.03	0.1	858.7	813.1	14.4	857.0
$k=6$	20.0	7	0.008	0.05	917.2	893.9	12.5	915.9

The ν energy distribution function $f_\nu(E_\nu) = \frac{1}{1-e^{(E_\nu-\mu_\nu^*)/T}}$, with $\mu_{\nu_{\mu,\tau}} = \mu_{\bar{\nu}_{\mu,\tau}} = 0$ and $\mu_{\bar{\nu}_e}^* = -\mu_{\nu_e}^*$

The average energy for muon/tau ν's $\langle E_\nu \rangle = \pi T$, while for the electron ν's $\langle E_\nu \rangle = (3/4)\mu_\nu^*$

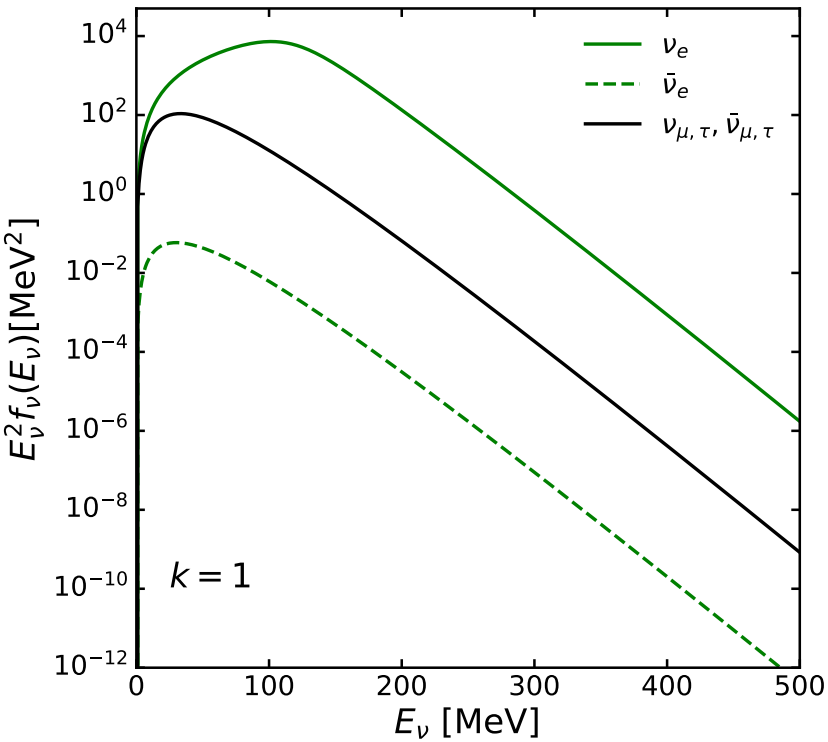

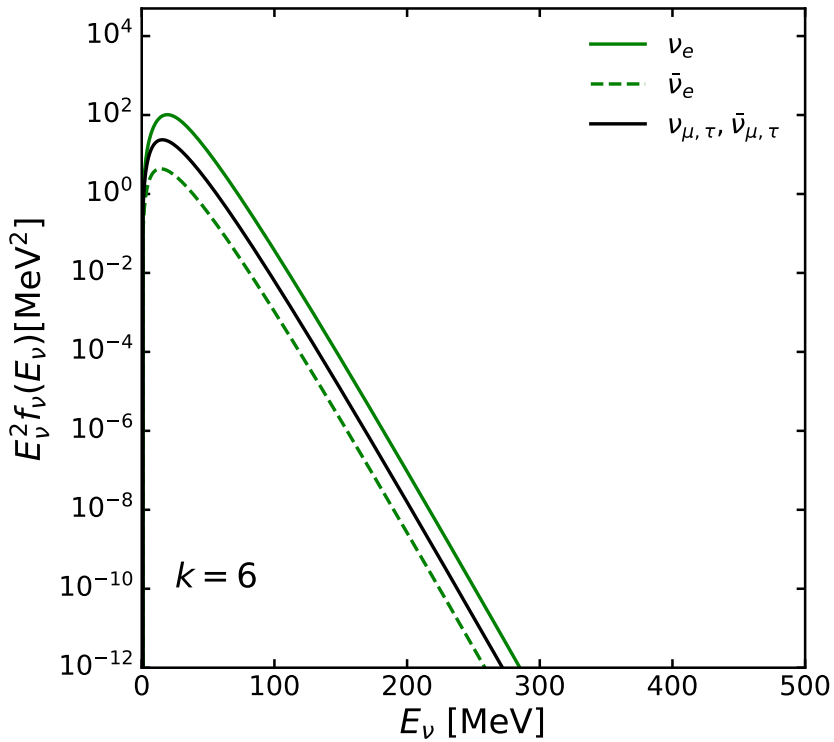

Effective nucleon masses and chemical potentials

Considering the TM1 model for a $18\,M_\odot$ progenitor in a relativistic mean field approach:

- The baryonic density, n_B, temperature, T, and electron fraction, Y_e, derived by *Fischer et al., PRD 85 (2012) 083003*
- The effective nucleon masses, $m_N^\star$, and the neutrino and nucleon effective chemical potentials, $\mu_{\nu_e}^*, \mu_n^*, \mu_p^*$ obtained by Cerdeño, **Cermeño**, Pérez-García and Reid, PRD 104 (2021) 063013
- $\mu_{\nu_e}^*$ is obtained solving the equilibrium equation that involves effective meson fields: $\mu_n^* + \mu_{\nu_e}^* = \mu_p^* + \mu_e^* + 2g_\rho\langle\rho\rangle$, where ρ is an effective field responsible of the strong interaction

	R (km)	T (MeV)	n_B(fm^{-3})	Y_e	μ_n^* (MeV)	μ_p^* (MeV)	$\mu_{\nu_e}^*$ (MeV)	$m_N^\star$ (MeV)
$k=1$	5.0	15	0.5	0.3	496.6	405.4	114.6	249.6
$k=2$	7.5	20	0.3	0.28	530.0	458.3	102.7	384.9
$k=3$	10.0	28	0.15	0.25	656.5	601.9	79.9	599.4
$k=4$	15.0	33	0.06	0.2	779.8	723.0	29.0	786.0
$k=5$	17.5	18	0.03	0.1	858.7	813.1	14.4	857.0
$k=6$	20.0	7	0.008	0.05	917.2	893.9	12.5	915.9

TABLE I. Values of neutron effective chemical potential, μ_n^*, proton effective chemical potential, μ_p^*, electron neutrino effective chemical potential, μ_ν^*, and nucleon effective mass, $m_N^\star$, for the spherical shells (labeled by the index k and defined by an outer radius R) that we consider at 1 s after bounce, with a baryonic density, n_B, temperature, T and electron fraction, Y_e. Temperatures, densities and electron fraction are taken from Ref. [45].

Effective nucleon masses and chemical potentials

The equation of state of nuclear matter is constructed using the relativistic mean field (RMF) theory with the TM1 parameter set *Sugahara and H. Toki, Nucl. Phys. A 579 (1994) 557, Shen et al., Nucl. Phys. A 637 (1998) 435*

- In the RMF approach baryons are considered Dirac quasiparticles moving in classical meson fields and the field operators, ϕ, are replaced by their expectation values, $\langle\phi\rangle$
- The TM1 model is a representative example where the set of parameters used can smoothly connect low and high density regions in the dynamical stellar description
- The presence of an effective nucleon mass and effective chemical potential is due to the non vanishing values of the Lorentz scalar meson, $\langle\sigma\rangle$, Lorentz vector, $\langle\omega_\mu\rangle$, and vector-isovector, $\langle\vec{\rho}_\mu\rangle$, meson fields

The effective nucleon mass $m_N^* = m_N - g_{\sigma N}\langle\sigma\rangle$

Effective nucleon chemical potentials, $\mu_i^* = \mu_i - g_{\omega N}\langle\omega\rangle - g_{\rho N} t_{3i}\langle\rho\rangle$ $(i = n, p)$

$g_{\sigma N}$, $g_{\omega N}$, and $g_{\rho N}$ are dimensionless constants that couple nucleons to the σ, ω, and ρ mesons
t_{3i} is the third component of the isospin of the proton or the neutron, $i = p, n$

This parameter set includes self-interaction terms from scalar, vector and vector-isovector mesons in non isospin symmetric nuclear matter at finite temperature

TM1 interaction terms are constrained by the nuclear masses, radii, neutron skins and their excitations

When applied to the derived proto-NS, the mass-radius diagram allows to fulfil the subsequent two solar mass constraint from recent observations of older objects.

Relativistic mean field theory lagrangian

The relativistic mean field theory lagrangian

Sugahara and H. Toki, Nucl. Phys. A 579 (1994) 557, Shen et al., Nucl. Phys. A 637 (1998) 435

$$\mathcal{L}_{RMF} = \bar{\psi}\left[i\gamma_\mu\partial^\mu - M - g_\sigma\sigma - g_\omega\gamma_\mu\omega^\mu - g_\rho\gamma_\mu\tau_a\rho^{a\mu} - e\gamma_\mu\frac{1-\tau_3}{2}A^\mu\right]\psi$$
$$+ \frac{1}{2}\partial_\mu\sigma\partial^\mu\sigma - \frac{1}{2}m_\sigma^2\sigma^2 - \frac{1}{3}g_2\sigma^3 - \frac{1}{4}g_3\sigma^4$$
$$-\tfrac{1}{4}W_{\mu\nu}W^{\mu\nu} + \tfrac{1}{2}m_\omega^2\omega_\mu\omega^\mu + \tfrac{1}{4}c_3\left(\omega_\mu\omega^\mu\right)^2$$
$$-\tfrac{1}{4}R^a_{\mu\nu}R^{a\mu\nu} + \tfrac{1}{2}m_\rho^2\rho^a_\mu\rho^{a\mu} - \tfrac{1}{4}F_{\mu\nu}F^{\mu\nu},$$

where

$$W^{\mu\nu} = \partial^\mu\omega^\nu - \partial^\nu\omega^\mu,$$
$$R^{a\mu\nu} = \partial^\mu\rho^{a\nu} - \partial^\nu\rho^{a\mu} + g_\rho\epsilon^{abc}\rho^{b\mu}\rho^{c\nu},$$
$$F^{\mu\nu} = \partial^\mu A^\nu - \partial^\nu A^\mu.$$

The nucleon field ψ having the mass M interacts with σ, ω_μ and ρ^a_μ mesons and the photon field A_μ.

Self-coupling terms with the coupling constants g_2 and g_3 for the σ meson and with the coupling constant c_3 for the ω meson

The coupling strengths, g 's, and the meson masses, m 's, are the parameters of this theory.

Different parameter sets for the Lagrangian

Sugahara and H. Toki, Nucl. Phys. A 579 (1994) 557

Table 2
The parameters of the lagrangian determined by the least-squares fitting procedure are listed under TM1 for the heavy nuclei and TM2 for the light nuclei. For comparison, the parameters of NL1 and NL-SH are also listed under the column of NL1 and NL-SH, respectively

	TM1	TM2	NL1	NL-SH
M (MeV)	938.0	938.0	938.0	939.0
m_σ (MeV)	511.198	526.443	492.250	526.059
m_ω (MeV)	783.0	783.0	795.359	783.0
m_ρ (MeV)	770.0	770.0	763.0	763.0
g_σ	10.0289	11.4694	10.1377	10.444
g_ω	12.6139	14.6377	13.2846	12.945
g_ρ	4.6322	4.6783	4.9757	4.383
g_2 (fm^{-1})	−7.2325	−4.4440	−12.1724	−6.9099
g_3	0.6183	4.6076	−36.2646	−15.8337
c_3	71.3075	84.5318	0.0	0.0

Relation between ν emission time and diffusion time

- At the onset of the cooling phase (~ 1 s after the bounce), the luminosity is of the order of 10^{52} erg s^{-1} for each ν and $\bar{\nu}$ species
- The outer layers cool down fast, the neutrinosphere recedes to smaller radii and the luminosity quickly drops
- The neutrino emission is backed up with the diffusion of ν's from the inner layers. Due to multiple scattering, ν's take a sizable time to reach the outer layers of the proto-NS, from where they are radiated out with a time scale of
  Janka arXiv: 1702.08713. In 'Handbook of Supernovae,' Springer

$$t_{\text{signal}} \sim \frac{3}{\pi^2} \frac{E_{th}^{tot}}{2E_{th}^{\nu}} R_{ns}^2 \left\langle \frac{1}{\lambda} \right\rangle \sim 10\, s,$$

- E_{th}^{tot} and E_{th}^{ν} are the total baryon and neutrino thermal energies, $E_{th}^{tot}/(2E_{th}^{\nu}) \sim 10$
- $\langle 1/\lambda \rangle$ the average of the inverse of the neutrino mean free path
- $R_{ns}^2 \langle 1/\lambda \rangle$ (where R_{ns} is the radius of the neutrinosphere) gives the time scale of the diffusion of a single particle with a velocity of light and with random walk steps of λ
- In order to fullfil $t_{\text{signal}} \sim 10$ s, $R_{ns}^2 \langle 1/\lambda \rangle \sim 3\,\text{s}/c$. From our calculation we get $R_{ns}^2 \langle 1/\lambda \rangle \sim 2.9\,\text{s}/c$ for electron neutrinos and $1.3\,\text{s}/c$ for muon and tau neutrinos

Muon production in SN in the SM

- The proto-NS may reach $T \sim 50$ MeV before it is cooled by ν diffusion (first 10 s)
- The proto-NS is born with a significant electron to baryon number ratio (from the core of the progenitor star) but no initial muon or tau population
- A net excess of e^- over e^+ occurs due to the high initial electron fraction compensating the positive charge of the protons
- Electrons highly degenerate with a chemical potential $\mu_e > m_\mu$
- The thermal distribution of photons and ν reach well beyond 100 MeV

Under these conditions μ^- and μ^+ are produced via

$$e^- + e^+ \longrightarrow \mu^- + \mu^+, \quad \gamma + \gamma \longrightarrow \mu^- + \mu^+,$$
$$\bar{\nu}_e + e^- \longrightarrow \bar{\nu}_\mu + \mu^-, \quad \nu_e + e^+ \longrightarrow \nu_\mu + \mu^+,$$
$$\nu_\mu + n \longrightarrow p + \mu^-, \quad \bar{\nu}_\mu + p \longrightarrow n + \mu^+$$

Net muon population in SN in the SM

- Once core-collapse SN is initiated, e^- and p in the progenitor combine and ν_e quickly diffuse out of the star, decreasing the net lepton number $\Rightarrow$ neutron-rich core
- Due to the excess of e^- over e^+ as well as the one of neutrons over protons, an excess of μ^- over μ^+ is built up
- Due to weak magnetism corrections, the interaction cross section for $N + \nu \longrightarrow N + \nu$ is slightly larger than for $N + \bar{\nu} \longrightarrow N + \bar{\nu} \Rightarrow \bar{\nu}$ diffuse out of the star faster than $\nu \Rightarrow \mu_\nu \neq 0$
- $\bar{\nu}_\mu$ diffuse out of the star faster than $\nu_\mu \Rightarrow$ net ν_μ population over $\bar{\nu}_\mu$ population $\Rightarrow$ increase of the net μ^- population over μ^+

The process of muonization that leads to an excess of μ^- over μ^+ in the final NS is facilitated by the previous reactions as well as $\nu_\mu + n \rightleftarrows p + \mu^-$, $\bar{\nu}_\mu + p \rightleftarrows n + \mu^+$ and

$\nu + \mu^- \rightleftarrows \nu' + \mu^{-'}$	$\nu + \mu^+ \rightleftarrows \nu' + \mu^{+'}$
$\nu_\mu + e^- \rightleftarrows \nu_e + \mu^-$	$\bar{\nu}_\mu + e^+ \rightleftarrows \bar{\nu}_e + \mu^+$
$\nu_\mu + \bar{\nu}_e + e^- \rightleftarrows \mu^-$	$\bar{\nu}_\mu + \nu_e + e^+ \rightleftarrows \mu^+$
$\bar{\nu}_e + e^- \rightleftarrows \bar{\nu}_\mu + \mu^-$	$\nu_e + e^+ \rightleftarrows \nu_\mu + \mu^+$
$\nu_\mu + n \rightleftarrows p + \mu^-$	$\bar{\nu}_\mu + p \rightleftarrows n + \mu^+$

Effect of a net muon number density on the profiles

Negligible effect of the net muon population in the temperature and density profiles *Bollig et al., PRL 125 (2020) 051104*

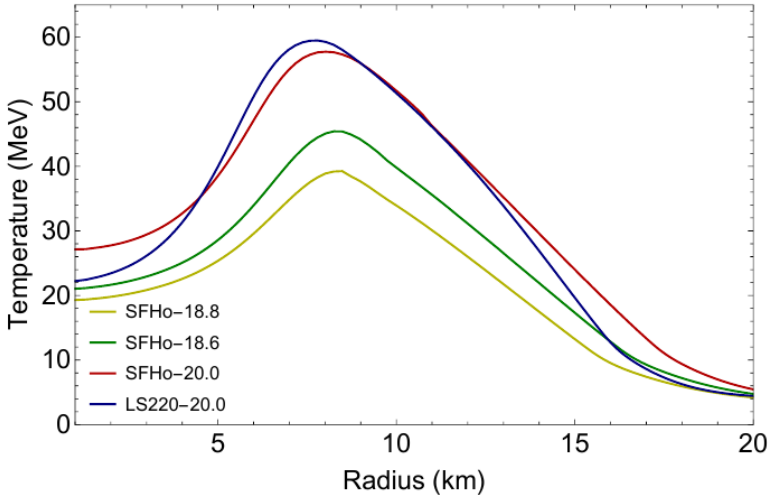

FIG. 1: Temperature profile for various models at 1 s post-bounce.

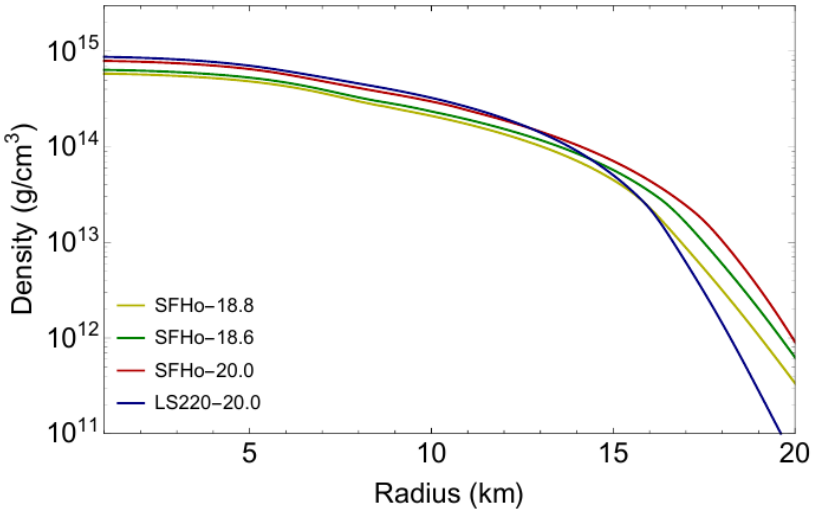

FIG. 2: Density profile for the models corresponding to Fig. 1

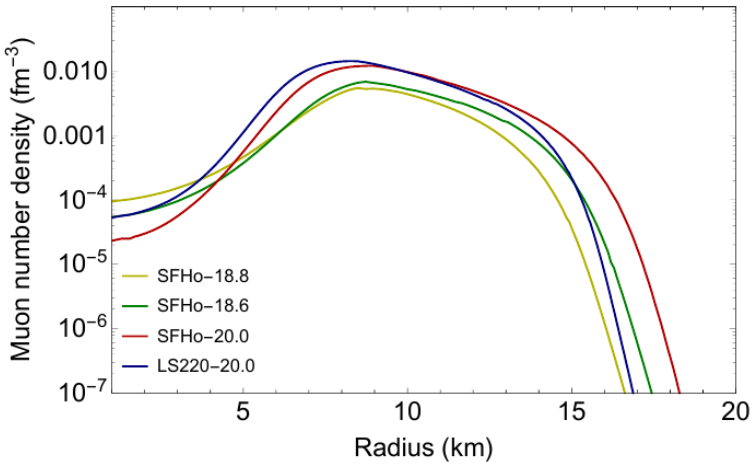

FIG. 3: Muon number density. Note that despite large differences in peak temperature, the muon number density does not change by more than an order of magnitude in the relevant region of high muon density ($5\,\mathrm{km} \lesssim r \lesssim 15\,\mathrm{km}$).

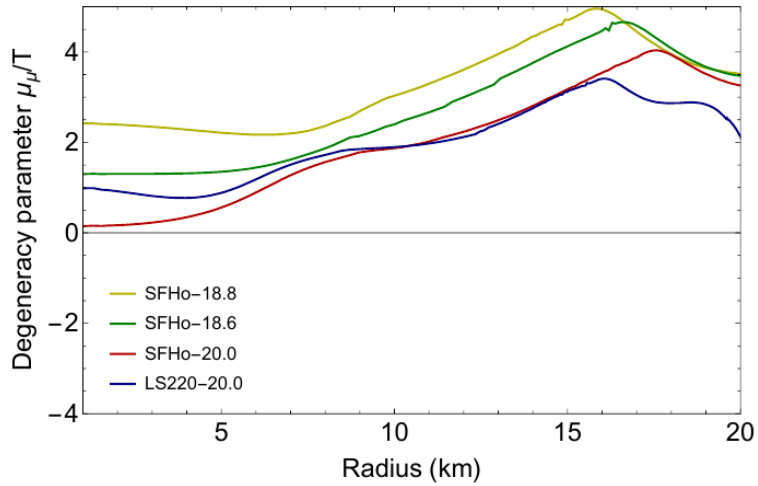

FIG. 4: Muon degeneracy parameter μ_μ/T for various profiles. This ratio never exceeds a small $\mathcal{O}(1)$ value in the relevant region of high muon density ($5\,\mathrm{km} \lesssim r \lesssim 15\,\mathrm{km}$).

Weak magnetism effect on μ_{ν_μ} and μ_{ν_τ}

Horowitz, PRD 65 (2002) 043001

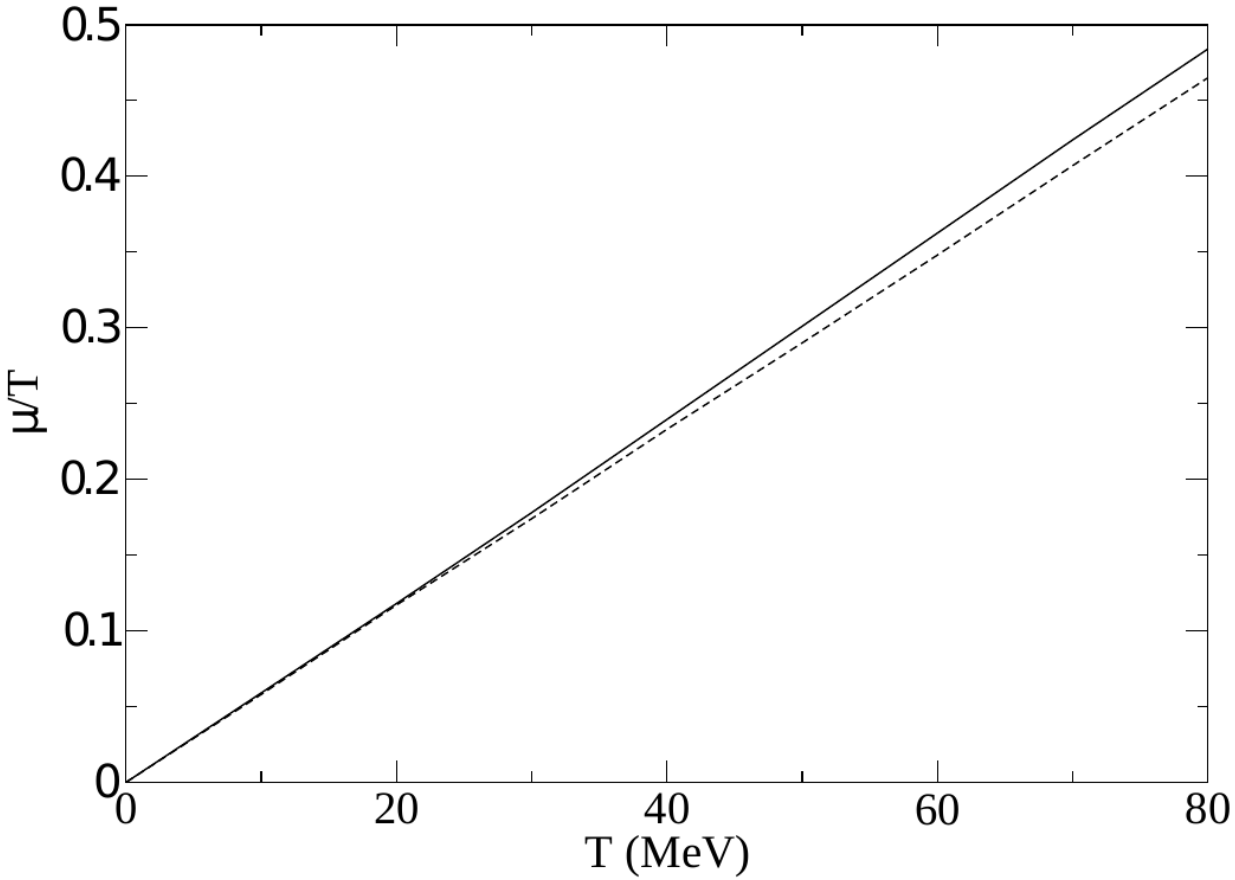

FIG. 3. Muon or Tau neutrino chemical potential over temperature μ_{ν_x}/T versus T for matter in steady state equilibrium. The solid line is the full result from the solution to Eq. (43) while the dashed line is correct to lowest order in k/M and μ/T, Eq. (44)